



BUILDING BLOCKS FOR TIME-RESOLVED LASER EMISSION IN
MID-INFRARED QUANTUM WELL LASERS

THESIS

Gabriel D. Mounce, First Lieutenant, USAF
AFIT/GE/ENP/03-01

DEPARTMENT OF THE AIR FORCE
AIR UNIVERSITY
AIR FORCE INSTITUTE OF TECHNOLOGY

Wright-Patterson Air Force Base, Ohio

APPROVED FOR PUBLIC RELEASE; DISTRIBUTION UNLIMITED

The views expressed in this thesis are those of the author and do not reflect the official policy or position of the United States Air Force, Department of Defense, or the United States Government.

AFIT/GE/ENP/03-01

Building Blocks For Time-Resolved Laser Emission In Mid-Infrared
Quantum Well Lasers

THESIS

Presented to the Faculty
Department of Engineering Physics
Graduate School of Engineering and Management
Air Force Institute of Technology
Air University
Air Education and Training Command
In Partial Fulfillment of the Requirements for the
Degree of Master of Science in Electrical Engineering

Gabriel D. Mounce, B.S.
First Lieutenant, USAF

25 March 2003

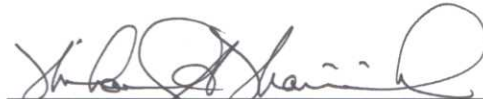
APPROVED FOR PUBLIC RELEASE; DISTRIBUTION UNLIMITED

AFIT/GE/ENP/03-01

Building Blocks For Time-Resolved Laser Emission In Mid-Infrared
Quantum Well Lasers

Gabriel D. Mounce, B.S.
First Lieutenant, USAF

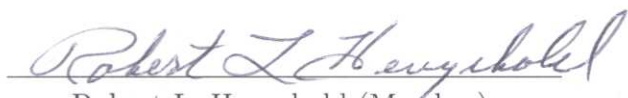
Approved:



Michael A. Marciak (Chairman)

14 Mar 03

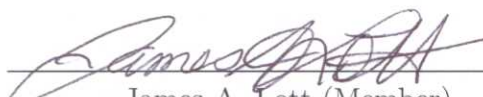
date



Robert L. Hengehold (Member)

14 Mar 03

date



James A. Lott (Member)

14 MARCH 2003

date

Acknowledgements

This project, the AFIT curriculum, and life as a military student have been the toughest challenges I've faced so far. Many thanks are in order to those people who helped to get me through it. First and foremost I want to sincerely thank my advisor, LtCol Michael Marciniak, whose guidance, encouragement, and flexibility allowed me to successfully complete the program. His continued faith in me was instrumental in my achieving a Master's degree. I would like to thank LtCol James Lott and Professor Robert Hengehold for their technical support and advice. To Greg Smith, Mike Ranft, and Rick Patton I owe considerable thanks for their never-ending assistance in the lab and their ability to keep things running in spite of myself. Other key players that I would not have got along without are Nathan Abel and Kevin Cumblidge whose assistance in the lab allowed me to keep up with my course work. My "computer lab buddies" also deserve thanks for keeping my spirits high.

I want to thank those who supported this work to include Dr. George Turner of MIT/Lincoln Labs and Dr. Ron Kaspi, Dr. Andrew Ongstad, and Mr. Mike Tilton of AFRL/DELS who supplied semiconductor samples and technical advice. Additionally, I want to thank Bill Siskaninetz of AFRL/SND for processing the samples.

Finally, all my love and deepest gratitude goes to my wife for her never-ending encouragement, undying patience, and eternal support. I could not have made it without her. And lastly, thanks be to God for watching over me and getting me through.

Gabriel D. Mounce

Table of Contents

	Page
Acknowledgements	iv
List of Figures	vii
List of Tables	xi
List of Abbreviations	xii
Abstract	xiii
I. Introduction	1-1
1.1 Motivation	1-1
1.2 Background	1-2
1.3 Problem Statement	1-3
1.4 Approach	1-4
1.5 Scope	1-4
1.6 Main Results	1-4
1.7 Thesis Overview	1-5
II. Background	2-1
2.1 Quantum Wells	2-1
2.2 Structure Types	2-4
2.3 Lasing Condition	2-5
2.4 Laser Cavity	2-7
2.5 Ghost Modes	2-10

	Page
III. Experiment	3-1
3.1 Upconversion Theory	3-1
3.2 Experimental Setup	3-4
3.2.1 Laser Source	3-4
3.2.2 Beam Paths	3-8
IV. Samples and Sample Preparation	4-1
4.1 Sample Description	4-1
4.2 Sample Preparation - Etching	4-7
4.3 Sample Preparation - Cleaving	4-8
V. Results and Analysis	5-1
5.1 Modelling Results	5-1
5.2 PL Results	5-2
5.3 Spontaneous Emission Results	5-4
5.4 Stimulated Emission Results	5-8
5.5 Lasing Results	5-14
5.6 Gain Calculation	5-14
5.7 Upconversion Results	5-22
VI. Conclusion	6-1
6.1 Summary	6-1
6.2 Future Work	6-2
Appendix A. Calculation of Non-Linear Crystal Tilt Angle	A-1
Appendix B. Gain Calculation Programs for TE and TM Modes . .	B-1
Bibliography	BIB-1
Vita	VITA-1

List of Figures

Figure	Page
2.1. (a) Schematic energy diagram of a semiconductor QW structure. E_a and E_b are the energy gaps that make up the barriers and well. E_1 and E_2 are the first two energy states confined in the well of width L. (b) Density of States in a quantum well and bulk material. The dashed curve represents the 3-D density of states for bulk material while the solid line is the 2-D density states for a particle confined to a quantum well. [30]	2-2
2.2. Type-I and type-II multiple quantum wells. Type-I has spatially aligned quantum wells. Type-II has spatially offset quantum wells.	2-4
2.3. Active region layer formed between wider bandgap cladding layers. The lower indices of refraction of the cladding layers confine optical emission. [30]	2-5
2.4. Three-layer slab-waveguide and zig-zag ray model [2].	2-8
2.5. Refractive indices and field profiles in a three-layer dielectric slab waveguide [2].	2-9
2.6. Layer schematic of laser device showing “ghost” modes (red) and active region mode (blue). Red arrows are ray traces representing “ghost” mode oscillation and blue arrows represent main lasing mode oscillation. [23]	2-10
2.7. Plot of quantum efficiency versus cavity length in a antimony-based QW device. The overall QE is seen to be higher with “ghost” modes present (+) than without (\triangle). [23]	2-11
2.8. Effective index, n_{eff} , and modal gain, G_{mod} , plots versus cap layer thickness, d for two cladding layer thicknesses of (a) 0.6 μm and (b) 0.8 μm . Resonance points shown where two TE mode branches of n_{eff} plots come close to intersecting. [14]	2-13

Figure	Page
3.1. Wave mixing resulting in the time resolution of the luminescence. (a) Depicts the luminescence curve over time. (b) Represents the pump beam at some delay time τ . [18]	3-2
3.2. Upconverted signal in terms of wavevectors [18].	3-3
3.3. Schematic of experimental setup showing the cryogenic mount, source leg, pump leg, and signal beam [12].	3-6
3.4. (a) Pulse width of Ti:Sapphire laser. FWHM is measured to be $\Delta t_m = 207$ fs. The actual pulse width is $\Delta t_a = 134$ fs after multiplying by the correction factor 0.648. (b) Spectral width of Ti:Sapphire pulse of 2.5 nm.	3-7
3.5. Photoluminescence configuration. The flat surface of the sample mount is positioned normal to the off-axis, parabolic mirror. The photoluminescence generated is collected by a series of CaF_2 lenses and sent to a spectrometer for evaluation. [12]	3-11
3.6. Laser configuration. The laser source beam is directed into the cryostat from the side, passing through a 200 mm biconvex lens and a 100 mm cylindrical lens forming a horizontal stripe. The surface normal of the cold finger is positioned at a slight angle to the incoming beam.	3-12
3.7. Laser source focused to a horizontal stripe. Profile along x axis shows a beam diameter at the $1/e^2$ point of 2.049 mm. . . .	3-13
3.8. Experimental set up in the TRPL experiment. The Ti:Sapphire laser creates a 130 fs pulse that is split into two paths. The laser signal beam travels through a delay stage before exciting the sample. Luminescence is collected and mixed with the pump beam in the KTA crystal. The upconverted beam is then directed to the spectrometer and photon counter. [12]	3-14
4.1. Sample 201-056 energy band and refractive index diagram drawn to scale. This sample is a type-II, dilute waveguide structure. [18, 27, 35, 38]	4-2

Figure		Page
4.2.	Energy band and refractive index diagram for samples R1-73 and R2-43 drawn to scale. These samples are type-II, dilute waveguide structures. [17, 23, 27, 38]	4-3
4.3.	Sample R0-62 energy band and refractive index diagram drawn to scale. This sample is a type-II, tight waveguide structure. [17, 23, 29, 38]	4-4
4.4.	Sample B energy band and refractive index diagram drawn to scale. This sample is a type-I, tight waveguide structure. [12, 35]	4-5
4.5.	Tight waveguides having cladding layers shown in gray and dilute waveguide having no cladding layers.	4-6
4.6.	Shape of GaSb test piece used for etch study with approximate locations of 1813 photoresist.	4-8
5.1.	Model of TE modes in sample R1-73. Only ghost modes are predicted as shown by the two lowest loss modes. [23] . . .	5-1
5.2.	Model of TE modes in sample R2-43. Again, only ghost modes are predicted as shown by the two lowest loss modes. [23] . .	5-2
5.3.	PL Spectra of the five different samples investigated. Relative intensities are not to scale.	5-3
5.4.	Spectra of Sample R0-62 taken as the spectrometer slit width is varied at a pump power of 720mW and temperature of 77K. No lasing or mode development is seen.	5-5
5.5.	Spectra of Sample R1-73 taken as the spectrometer slit width is varied at a pump power of 720mW and temperature of 77K. No lasing or mode development is seen.	5-6
5.6.	Spectra of Sample R2-43 taken as the spectrometer slit width is varied at a pump power of 720mW and temperature of 77K. No lasing or mode development is seen.	5-7
5.7.	Spectra of Sample 201-056 taken at 80 and 10 K with 2.37 W excitation power. Longitudinal Mode development is seen along the crests of the two spectra.	5-9

Figure		Page
5.8.	Close-up of spectra showing a high degree of mode overlap, confirming repeatability and thus mode formation. The longitudinal mode spacing is 170.75 ± 1.36 GHz.	5-10
5.9.	Spectrum of Sample B taken at 77 K with 2.37 W excitation power. Longitudinal mode development is seen along the crests of the spectrum. The mode spacing is 169.37 ± 0.58 GHz. . . .	5-11
5.10.	Spectra of Sample 201-056 taken as the source beam power is decreased from 2.37 W to 0.1 W.	5-12
5.11.	Close-up of Sample 201-056 spectra showing longitudinal modes ceasing to occur at 0.2 W.	5-13
5.12.	Spectra of Sample B taken at temperatures of 77K and 5K. Lasing is seen to occur at 5K as evident by the large intensity spike.	5-15
5.13.	Spectra of Sample B taken at a temperature of 8K under varying pump powers. Saturation occurs at a pump power of 1.5 W and laser output is decreased at higher pump powers.	5-16
5.14.	Gain curves of Sample 201-056 at 80K for the TE and TM modes. .	5-19
5.15.	Gain curves of Sample B at 77K for the TE and TM modes. .	5-20
5.16.	Gain curves of Sample B at 8K for the TE and TM modes. .	5-21
5.17.	TRPL signal of sample B on 7 Nov 02.	5-23

List of Tables

Table	Page
3.1. Calculated spot sizes of 200 mm and 300 mm lenses in the x, y, and radial directions.	3-8
5.1. Characteristics of samples under investigation.	5-2
5.2. Spectrometer slit widths and grating increments used in data acquisition of emission spectra.	5-4

List of Abbreviations

Abbreviation		Page
DH	Double-Heterostructure	1-1
QW	Quantum Well	2-1
MQW	Multiple Quantum Wells	2-4
TEM	Transverse Electro-Magnetic	2-7
QE	Quantum Efficiency	2-11
TRPL	Time-Resolved Photoluminescence	3-1
PL	Photoluminescence	3-1
SFG	Sum Frequency Generation	3-1
KTA	KTiOAsO ₄	3-2
SHG	Second Harmonic Generation	3-5
FWHM	Full Width at Half Maximum	3-5
PMT	Photo-Multiplier Tube	3-5
MIT	Massachusetts Institute of Technology	4-1
AFRL/DE	Air Force Research Lab/Directed Energy Directorate . .	4-1
AFRL/SND	AFRL, Sensors Directorate, Aerospace Components Division	4-7
RIE	Reactive Ion Etch	4-7
sccm	Standard Cubic CM	4-8
OPO	Optical Parametric Oscillator	6-2

Abstract

The objective of this research is to improve the performance of mid-infrared semiconductor quantum-well lasers. Lasers operating in the mid-infrared are useful for many Air Force applications which include infrared (IR) countermeasures in particular. Countermeasure applications require lasers that are compact, and able to emit at high powers while operating at room temperature. Limits to power increases are seen in the transverse modal development of laser oscillation. These modes typically form in the waveguiding active region contributing to the laser output. However, competing modes outside of this region also develop when the confining structural layers have the right characteristics. These competing modes may draw power away from the main lasing mode, causing efficiency to drop. Therefore, theoretical models indicate that these “ghost” modes should be extinguished. The goal of this work is to incorporate antimony-based semiconductor laser devices into a time-resolved photoluminescence (TRPL) experiment to examine modal development immediately after excitation. TRPL utilizes a non-linear wave mixing technique known as frequency upconversion to resolve sub-picosecond luminescence occurrences after excitation. Modification to the experiment is performed to produce laser emission from five mid-IR semiconductor laser samples. Both spontaneous and stimulated emission spectra are recorded. Alignment of the experiment is also carried out to produce upconversion of the PL signal to prepare for the incorporation of laser emission.

InAs/InGaSb quantum well laser devices were studied in four categories: dilute and tight waveguide structures, and type-I and type-II energy-band geometries. Models are obtained to predict mode development and possible ghost mode resonance in the dilute waveguide case. It is seen here that dilute waveguides generate ghost modes because of the evanescent leakage and subsequent trapping of optical radiation in the cap and substrate layers. This data is then compared to the actual

behavior of the samples. Lasing is found to occur in the type-I, tight-waveguide case at low temperatures, while only sub-threshold emission is seen for the type-II dilute-waveguide. This is attributed to the absorption of the optical pump in the GaSb cap layer of the type-II device. Samples having no cap layers to prevent absorption showed only spontaneous emission as was predicted by modelling. The longitudinal mode spacing in emission spectra was measured and found to coincide with calculated values. Gain calculations were also performed using the Fabry-Perot resonances for the samples producing stimulated emission.

Building Blocks For Time-Resolved Laser Emission In Mid-Infrared Quantum Well Lasers

I. Introduction

Laser devices emitting in the infrared wavelength window of 3 to 5 μm are important to Air Force applications such as electronic countermeasure devices, trace gas detectors, laser radar, and for target recognition [1,5,7,10,20,22,24,34,39,40]. As such, devices that can produce high emission output with minimal power consumption while operating at room temperature are desired. Lead-salt structures produce such radiation, but they cannot operate at room temperature due to low thermal conductivity [6,20,40]. HgCdTe double-heterostructure (DH) devices have also produced emission in this window, but suffer from low thermal conductivity because of the high mobility of the Hg atoms [5,6,20]. Therefore, structures that are stable, compact, and able to produce this type of radiation at low threshold currents are required. Structures with such potential are III-V, antimony-based quantum-well lasers. These semiconductor structures show good physical and thermal characteristics, making them desirable for use in Air Force applications.

1.1 Motivation

Testing of this class and type of semiconductor device is now especially important to Air Force war fighters as new technology is needed for countermeasure systems in the defense of aircraft. Small, lightweight systems that can be mounted unobtrusively on aircraft and that can effectively defeat enemy anti-aircraft missiles are highly desired. Small, semiconductor laser devices are ideal for this purpose. Once fully realized, these devices would be mounted to provide all-aspect protection of aircraft using minimal power consumption. [31]

1.2 Background

To date, III-V materials have been used significantly in the manufacture of laser devices showing excellent results near $2 \mu\text{m}$. Emitting beyond this, however, has proven to be a challenge. The reasons for this are most readily attributed to the type of arrangement and composition of the laser structure. Understanding how these attributes affect the lasing process will give the knowledge needed to increase the lasing wavelength beyond this $2 \mu\text{m}$ barrier.

Increasing the performance of III-V semiconductor lasers requires understanding of how lasing develops within the structure. The devices studied here are antimony-based, strained multiple-quantum-well (MQW) structures. The strained quantum-well arrangement is devised to optimize carrier confinement, which is the key to achieving room temperature lasing at low threshold currents. Quantum wells are effective confinement structures because of the low energy states carriers see within the wells, as compared to the surrounding material. Therefore, carriers, once injected, are funnelled into the wells where they recombine, producing radiation. The thicknesses of the different layers of semiconductor material forming the wells, barriers (separation layers between wells), cladding regions (layers surrounding the well/barrier layers) and cap layers (for metal contacting) are engineered to achieve the best possible performance.

Lasing takes place in the active region made up of the quantum-well/barrier layers so it is necessary to understand how the thicknesses aid or detract from the lasing process. Research performed at the University of New Mexico has shown that different layer thicknesses cause different lasing modes to dominate within the active region. In particular, they find that normal TE modes outside the active region come into existence and compete with the lasing modes. These modes are referred to as “ghost modes” and are found to detract from the lasing process. They occur as the result of varying layer thicknesses within the device structure. This research shows that certain layers within the structure are coupled to one another,

i.e., the active region waveguide is coupled to the buffer-substrate layer waveguide or the active region waveguide is coupled to the cap layer waveguide. When energy is injected, these ghost modes develop taking energy from the lasing mode, which in turn requires more energy input to support lasing. [13–15]

It is shown that the ghost modes depend on the thicknesses of the coupled layers. Normal modes depend on the effective refractive index and on the modal gain. These parameters are used to find the resonance points of the normal modes. Resonance points depend on the layer thicknesses of outside coupled waveguides and on the thickness of separating layers. The resonance points determine where the normal modes are ghost modes and where they coincide with the lasing mode. The lasing mode does not correspond to a single normal mode, but to a series of different normal modes of increasing mode order. At each resonant point, the normal mode is part of the lasing mode (in the active region), contributing to output, or it forms outside the active region (ghost mode). In other words, the modal intensity peak varies in location within the laser structure at each resonant point. If this peak is in the active region, it is a lasing mode, otherwise it is a ghost mode. [13–15]

1.3 Problem Statement

Although calculated theoretically, the development of lasing and ghost modes in quantum-well structures is not well understood. Therefore, it is important to see how modes develop within the structure to determine what affect they have on the lasing process. We hypothesize that the dynamics of laser emission can be seen in the first few nanoseconds after lasing threshold is reached. By studying the spectral evolution of the lasing emission, modal dynamics can be studied which gives information necessary to optimize the structure for low threshold current and high output power.

1.4 Approach

To investigate how modes develop within the laser structure, a frequency upconversion experiment will be used. Upconversion is also known as sum frequency generation, where two incoming light waves are mixed within a nonlinear crystal to form a third. Upconversion will be used for this experiment because of its ability to render sub-picosecond resolution. This kind of temporal resolution is needed as radiative (lasing) processes occur in the first few nanoseconds after excitation. The experiment and experimental setup will be almost identical to that used by Captain Steve Gorski for his AFIT thesis where he performed frequency upconversion on photoluminescence emission [18]. This research attempts to use this technique on laser emission.

1.5 Scope

To utilize upconversion to see modal processes, the experiment is modified to incorporate laser structures. To do this, the semiconductor structures investigated are first characterized for peak emission. They are then formed into laser devices and inserted into the experiment. The experimental setup is next modified to stimulate lasing by altering the optical pump beam used to excite the devices. Finally, upconversion is verified using the luminescence setup to prepare for laser emission.

1.6 Main Results

The results of theoretical models are presented indicating that no detectable lasing is expected from the three samples having their cap layers removed. This is verified by luminescence data. The modification to the upconversion experimental setup was shown to produce stimulated emission from a type-I and type-II, antimony-based quantum-well structure. This setup was also shown to produce lasing in a type-I structure at low temperatures.

Upconversion was achieved using the photoluminescence of the type-I structure as a baseline. However, the signal detected was marginal which is attributed to poor optical alignment. No analysis of the signal was possible.

1.7 Thesis Overview

Chapter II provides the background theory pertaining to semiconductor laser devices, to include laser production and mode theory. Chapter III details the TRPL experiment, upconversion theory, and the three experimental setups used, which include modifications for inclusion of laser devices. Chapter IV presents the five semiconductor samples investigated including their material and structural makeup. This chapter also presents transformation of the samples into laser structures. The results and analyses of these efforts are included in Chapter V. Chapter VI summarizes the findings of experimentation and includes recommendations for future work.

II. Background

The key to attaining the magnitude of output power desired at room temperature in mid-IR semiconductor lasers is the confinement of optical carriers in such a way as to ensure radiative recombination. These carriers are electrons in the conduction band and holes in the valence band of a semiconductor that have the potential to recombine and produce a photon. The recombination of electrons and holes that does not produce radiation is known as non-radiative recombination. The type of carrier confining structures that are examined here are quantum wells.

2.1 Quantum Wells

A quantum well (QW), shown in Figure 2.1, is a double heterostructure whereby a narrow bandgap semiconductor is sandwiched between two higher bandgap semiconductors. This configuration forms a rectangular quantum potential well from the energy bands. When the thickness of the narrow bandgap material, L, is on the order of the de Broglie wavelength of a thermalized electron ($\lambda = h/p$, where h is Planck's constant and p is the momentum of the electron), quantum size effects occur forming quantized energy states within the well [28]. These states represent the probability of having an electron or hole in any respective position within the well and are found from the solution to the time independent Schrödinger wave equation in two dimensions. The resulting eigenvalues (energy states) are given by:

$$E(n, k_x, k_y) = E_n + \left(\frac{\hbar^2}{2m_{n,p}^*} \right) (k_x^2 + k_y^2) \quad (2.1)$$

where E_n is the n_{th} energy state of the z-component (normal to the well layer), $m_{n,p}^*$ is the electron or hole effective mass, \hbar is the reduced Planck's constant, and k_x and k_y are the crystal momentum in the unconfined x and y directions. [28, 30]

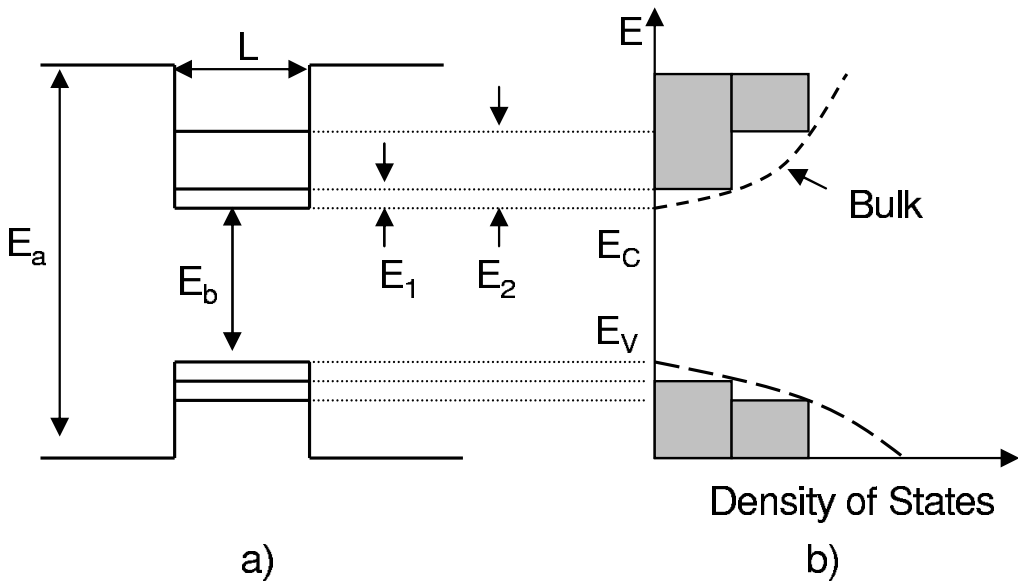


Figure 2.1 (a) Schematic energy diagram of a semiconductor QW structure. E_a and E_b are the energy gaps that make up the barriers and well. E_1 and E_2 are the first two energy states confined in the well of width L . (b) Density of States in a quantum well and bulk material. The dashed curve represents the 3-D density of states for bulk material while the solid line is the 2-D density states for a particle confined to a quantum well. [30]

The number of available quantum states in a given energy interval of a QW is given by the density of states function. Because of the quantized energy states in a QW, this function is

$$g(E)dE = [m_n^*/(\pi\hbar^2)] dE \quad (2.2)$$

which forms a staircase function beginning at the lowest energy states in the conduction and valence bands (shown in Figure 2.1). Because energy is quantized, there are no allowed states at other than the eigenvalue solutions. Thus, the function does not form a smooth parabolic band as in bulk material. This leads to wavelength emission being confined to narrow linewidths. [2, 28]

The experiment presented in Chapter III utilizes optical pumping to excite electrons into the conduction band of the compound semiconductor. Once excited, the electrons (and corresponding holes) are scattered into the wells because of the lower energy states that reside there. Thus, QW's are effective confinement structures, trapping carriers where they are more likely to recombine producing photons. The peak wavelength of light emitted is determined by the energy difference between the lowest level electron and hole energy levels within the wells. [2]

When excited, the carriers are put into a state of nonequilibrium. At equilibrium, the carrier densities are calculated using Fermi-Dirac statistics, which define the equilibrium level as the Fermi level. In nonequilibrium, the excited carriers quickly equilibrate with themselves, not the semiconductor crystal lattice putting them in a “quasi-equilibrium”. The nonequilibrium carrier distribution functions are therefore given by the “quasi-Fermi” functions

$$f_n(E) = \frac{1}{1 + \exp\left(\frac{E - E_{fn}}{k_B T}\right)} \quad (2.3)$$

$$1 - f_p(E) = \frac{1}{1 + \exp\left(\frac{E - E_{fp}}{k_B T}\right)} \quad (2.4)$$

for electrons and holes, respectively. Here, T is temperature, k_B is Boltzman's constant, E is energy, and E_{fn} and E_{fp} are the quasi-Fermi levels. These functions give the carrier concentration for any energy state within a semiconductor. [2]

2.2 Structure Types

As mentioned above, the narrow bandgap material form the wells. The wider bandgap material surrounding the well forms the barrier layers. In multiple quantum wells (MQW), a number of these well/barrier combinations are formed, one after another in alternating fashion (refer to Figure 2.2). MQW regimes are used to increase the overall gain of a device by consolidating the power produced from each individual well. This leads to greater output optical power on the one hand, but higher energy consumption on the other. A superlattice is formed in a MQW structure when the barrier layers are made thin enough to allow the electrons to tunnel through (quantum mechanically) causing the discrete energy levels of each well to broaden into miniature bands. This is known as wavefunction overlap.

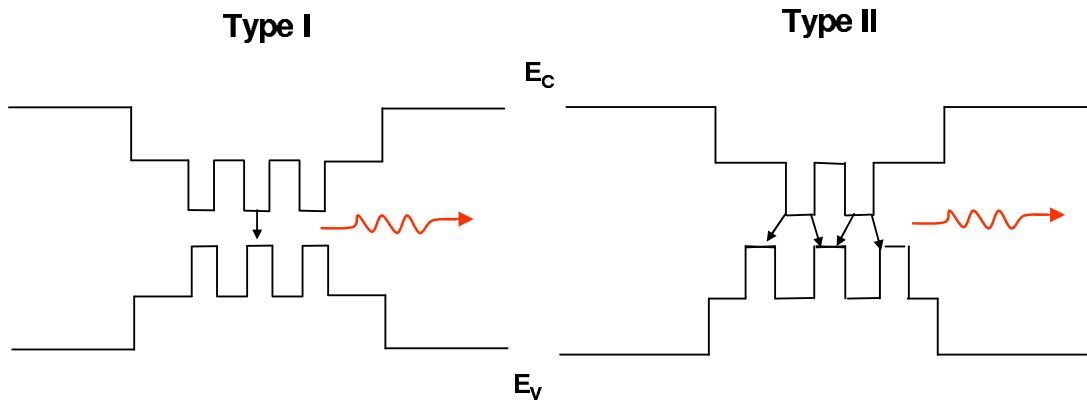


Figure 2.2 Type-I and type-II multiple quantum wells. Type-I has spatially aligned quantum wells. Type-II has spatially offset quantum wells.

Both type-I and type-II superlattice structures are used in this experiment. A type-I structure has spatially direct bandgap energies, while a type-II has spatially indirect band-gap energies (Figure 2.2) . [30]

The QW's and barriers form a section of the laser device called the active region, the region where light is produced. Surrounding the active region, another layer of semiconductor is grown, known as the cladding layers. These layers are higher in potential energy (wider bandgap) than the barriers and have lower indices of refraction, allowing the active region to act as a guide to the emitted photons, trapping them in this region. This active region forms the gain region as shown in Figure 2.3. [20,30]

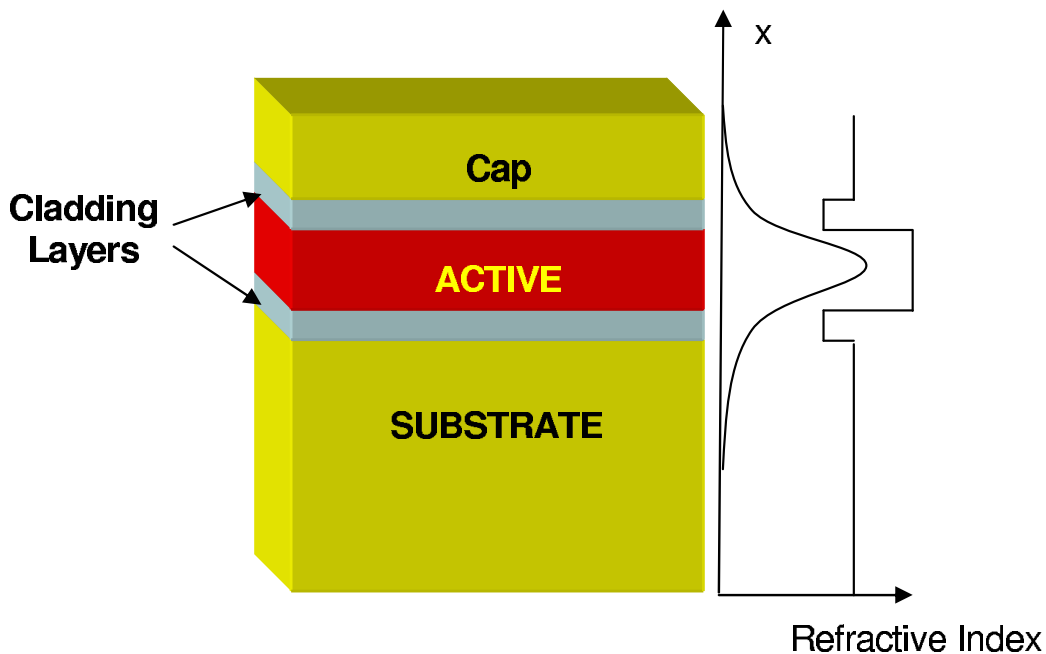


Figure 2.3 Active region layer formed between wider bandgap cladding layers. The lower indices of refraction of the cladding layers confine optical emission. [30]

2.3 Lasing Condition

Laser action and optical gain occur in a semiconductor because of the nonequilibrium of carriers that populate the bands. This state is attained as described above.

The absorption of incident photons is given by the absorption rate as

$$r_{abs} = P[1 - f_n(E_2)]f_p(E_1)N_p(E) \quad (2.5)$$

while the stimulated emission rate is given as

$$r_{st} = Pf_n(E_2)[1 - f_p(E_1)]N_p(E) \quad (2.6)$$

where P is the transition probability, N_p is the density of photons of energy E , and f_n and f_p are the Fermi functions given in equations 2.3 and 2.4. For lasing to occur, there must be more stimulated radiative processes than photon absorption processes, thus $r_{st} > r_{abs}$. This condition leads to $f_n(E_n) > f_p(E_p)$ where $E_n - E_p$ is the transition energy from the conduction band to the valence band. This condition causes population inversion: where the concentration of electrons in the conduction band is greater than the concentration of holes in the valence band. The gain, represented by stimulated downward transitions of carriers, should be at least equal to the losses, stimulated upward transitions, for lasing to occur. [2]

As the recombination rate increases from optical pumping, stimulated emission increases, building up the photon density. These photons stimulate further recombination causing light emission to grow. Since the radiation is comprised of both spontaneous and stimulated emission, multiple frequencies of light exist. Therefore, the lasing medium is placed in a Fabry-Perot cavity to selectively amplify one frequency. This cavity provides positive feedback for the selected frequency by producing a standing wave at that frequency. The Fabry-Perot cavity is formed by cleaving the semiconductor along two parallel crystal planes forming almost perfect mirrors. The initial light produced is amplified as it travels in the cavity between the mirrors and is fed back into the cavity as it reflects. Lasing happens when the gain from the medium overcomes the loss in the cavity for a roundtrip of light between

the mirrors. This threshold gain condition is represented by

$$g_{th} = \gamma + \frac{1}{2d} \ln \left(\frac{1}{R_1 R_2} \right) \quad (2.7)$$

where γ is the loss in the cavity, d is the cavity length, and R_1 and R_2 are the front and back mirror reflectivities. [2]

2.4 Laser Cavity

The general laser structure is made from multiple layers of semiconductor material as shown in Figure 2.3. Oscillation (production of the standing wave) in this kind of structure takes the form of transverse and longitudinal modes. The transverse modes are a result of photons being trapped by the cladding layers along the direction perpendicular to the layers of the semiconductor as seen in Figure 2.3. These modes are the propagating modes of the waveguide. Thus, the modes that are created in this direction are called transverse electromagnetic (TEM) modes. These modes are governed by the wavefunction solution to Maxwell's wave equation. The solution takes the form of a propagating wave

$$E(r, t) = E(r) e^{j(\omega t - \beta z)} \quad (2.8)$$

where β is the propagation constant for a wave moving in the z-direction. Substituting this equation into the Helmholtz equation where the y and z dimensions are approximated to infinity gives

$$\frac{\partial^2}{\partial x^2} E(x, y) + (k^2 n_l^2 - \beta^2) E(x, y) = 0 \quad (2.9)$$

with $l = 1, 2, 3$ for the three regions I, II, and III (reference Figure 2.4). Here k is the wavevector $2\pi/\lambda$ and $n_2 > n_3 > n_1$, where n_l is the index of refraction. For wave

confinement, the condition $kn_3 < \beta < kn_2$ must be satisfied and $n_2 > n_1, n_3$. This propagation regime produces β values that are eigenvalue solutions. [2]

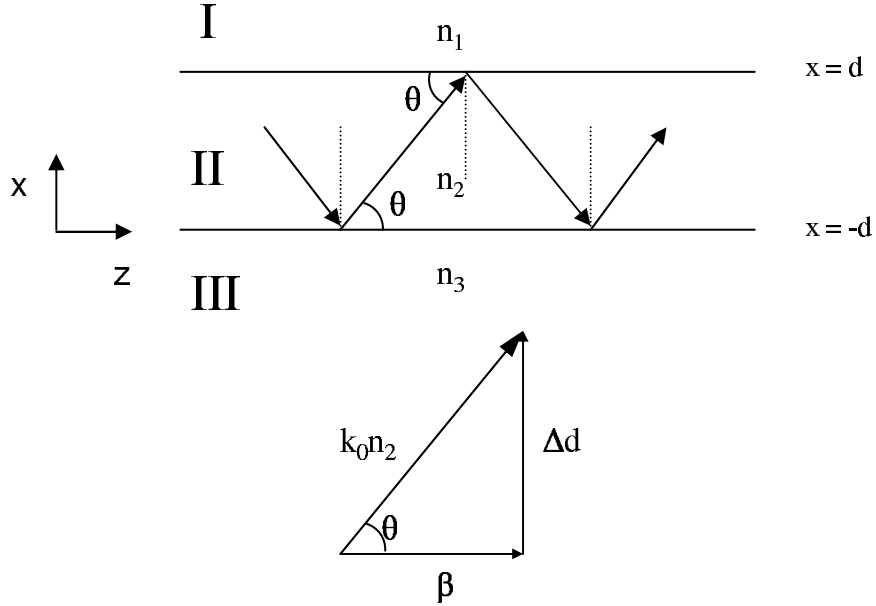


Figure 2.4 Three-layer slab-waveguide and zig-zag ray model [2].

The number of confined modes in the active region depend on the values of n_1 , n_2 , and n_3 , the frequency, and the active region thickness. Therefore, conditions exist describing which modes can be supported in the waveguide. For a symmetric waveguide where $n_1 = n_3$ and $n_2 > n_1$, the condition is

$$\Delta n = (n_2 - n_1) > \frac{m^2 \lambda^2}{16(n_1 + n_2) d^2}, m = 0, 1, 2, \dots \quad (2.10)$$

where d is the thickness of the active region. A similar expression exists for an asymmetric waveguide as

$$\Delta n = (n_2 - n_3) > \frac{(2m+1)^2 \lambda^2}{64(n_2 + n_3) d^2}, m = 0, 1, 2, \dots \quad (2.11)$$

where $n_3 \gg n_1$. A schematic of the symmetric case is shown in Figure 2.5. [2]

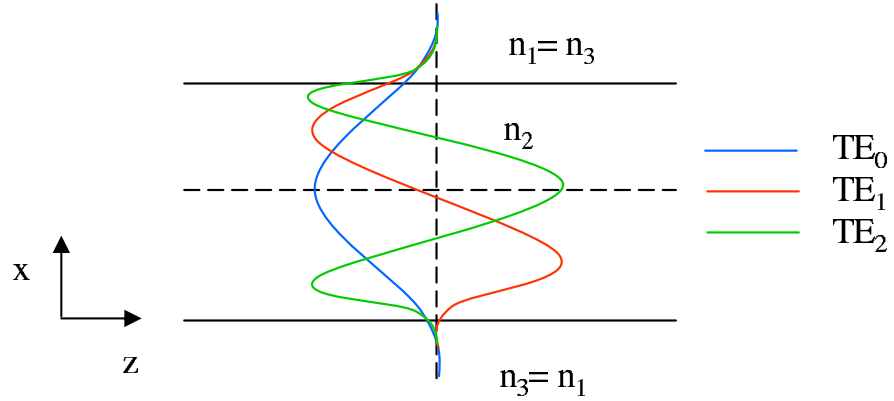


Figure 2.5 Refractive indices and field profiles in a three-layer dielectric slab waveguide [2].

Longitudinal modes are formed along the length of the active region parallel to the semiconductor layers. These modes define laser resonance. This is the process whereby photons generated in the active region oscillate along the length perpendicular to the cleaved “mirror” facets producing gain and thus laser emission. The cavity is resonant because only certain frequencies (wavelengths) of light are allowed within it. These resonant frequencies are governed by the cavity length d . The appropriate choice will stimulate a certain wavelength while damping all others. This condition is

$$d = q\lambda/2n \quad q = 1, 2, 3\dots \quad (2.12)$$

where λ is the wavelength, and n is the effective index of refraction within the active region. The resonant frequency follows from this expression as

$$v_q = qc/2nd \quad q = 1, 2, 3\dots \quad (2.13)$$

where c is again the speed of light. These frequencies are the longitudinal modes which are solutions to the Helmholtz equation with appropriate boundary conditions. The longitudinal mode spacing is obtained by rewriting this expression as $v_q 2nd = qc$

and differentiating to obtain

$$2d(v_q dn + ndv_q) = dqc \quad (2.14)$$

For adjacent modes, $dq = -1$ giving

$$dv_q = v_f = -\frac{c}{2nd} - \frac{v_q dn}{n} \quad (2.15)$$

also known as the frequency spacing. [4, 37]

2.5 Ghost Modes

As discussed above, transverse modes exist in the active region of the device of TE or TM type. Additional transverse modes exist in the device, as well, in layers outside the active region. This is due to the evanescent penetration of laser emission into these layers and the ensuing accumulation of such emission. These modes may become coupled to the lasing mode if the barrier layers separating them are thin enough. Specifically, cap and substrate layers, having waveguide properties themselves, are separated from the active region by the cladding layers. Modes that develop here can couple with active region modes depending upon the thickness of the cladding layers (reference Figure 2.6). These other modes are called “ghost”

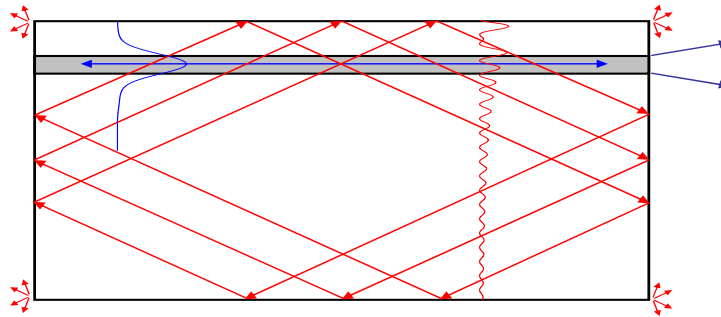


Figure 2.6 Layer schematic of laser device showing “ghost” modes (red) and active region mode (blue). Red arrows are ray traces representing “ghost” mode oscillation and blue arrows represent main lasing mode oscillation. [23]

modes [14]. The cladding layers are usually thin enough that optical penetration does indeed occur allowing mode coupling. This coupling becomes stronger if the ghost modes have the same longitudinal frequency and phase velocity as the active region modes (phase synchronism), and the mode volumes of the two are overlapping. Ghost modes are attributed with certain cases of high optical losses in certain laser modes [14]. It is theoretically calculated that, at some conditions of mode coupling, laser action can be prevented altogether. However, experimental results achieved by Kaspi *et al.* [22] have shown that “ghost” mode coupling increases the overall quantum efficiency (QE) as seen in Figure 2.7. Therefore, it is useful to understand the coupling process to determine its effect on the overall lasing process and to learn how to use it to enhance spectral selectivity. [14]

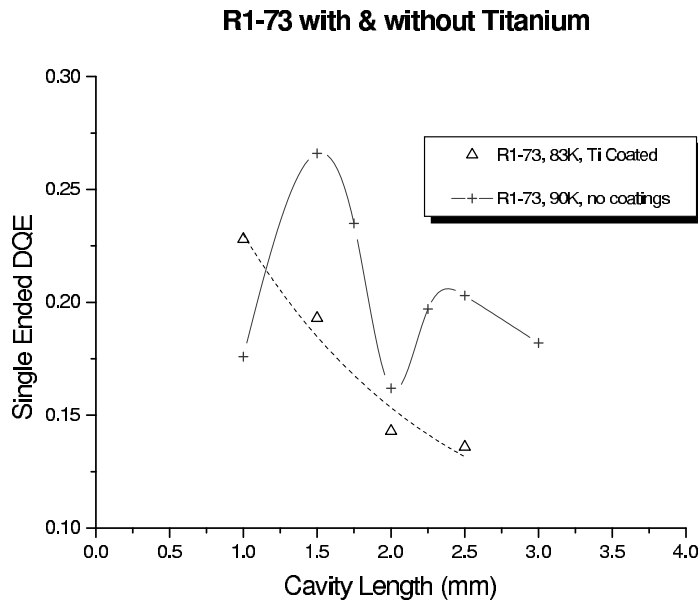


Figure 2.7 Plot of quantum efficiency versus cavity length in a antimony-based QW device. The overall QE is seen to be higher with “ghost” modes present (+) than without (Δ). [23]

To depict how modes interact, examples are used from theoretical calculations made by Eliseev *et al.* [14] for laser structures made from GaAs/InGaAs. Their

results are displayed in terms of the effective index, $n_{eff} = \text{Re}\beta/k$, where k is the wave number and β is the complex propagation constant, and the mode gain, $G_{mod} = 2\text{Im}\beta$. Each mode can be represented by its mode profile, its effective index, and its mode gain. For cap layer coupling, it is seen that because of its comparable thickness to that of the combined active/cladding layers, lower order TE modes exist. If this layer can be made thin enough, the laser mode can be made free of mode-coupling. As this layer increases, the ghost mode appears and coupling ensues, especially if the cap and active layers have close effective indices. As the cap layer increases, higher order modes become involved. To show this, n_{eff} and G_{mod} are both plotted versus the cap layer thickness, d , in Figure 2.8. [14]

The two sets of graphs shown are for two different cladding layer thicknesses. The upper graphs are plots of n_{eff} while the lower graphs are plots of G_{mod} . The thickness of the cladding layer defines where the branches (different TE modes shown) of the n_{eff} plots come close to touching. These spots on the graph define the coupling coefficient and are considered the coupling resonance points. Together, the two graph sets show how the cladding layer separating the active region and the cap layer affect mode coupling. The graphs show that at high coupling (corresponding to smaller cladding layers), the n_{eff} mode branches do not intersect, where at low coupling the branches are close to intersecting. The G_{mod} plots show intersections at points lower on the branches for high coupling and at points higher on the branches for low coupling. In the effective index plots, the vertical sections of the branches represent in-phase oscillations and the horizontal sections antiphase oscillations near the coupling resonance points. The active region lasing mode dominates along the horizontal sections of the branches meaning that sufficient mode gain can only occur at these cap layer thicknesses. [14]

Substrate mode coupling is similar to that of the cap layer except that the substrate is much thicker than the cap layer. This means that higher order modes will be coupled to the active mode. The substrate coupling also produces spectral

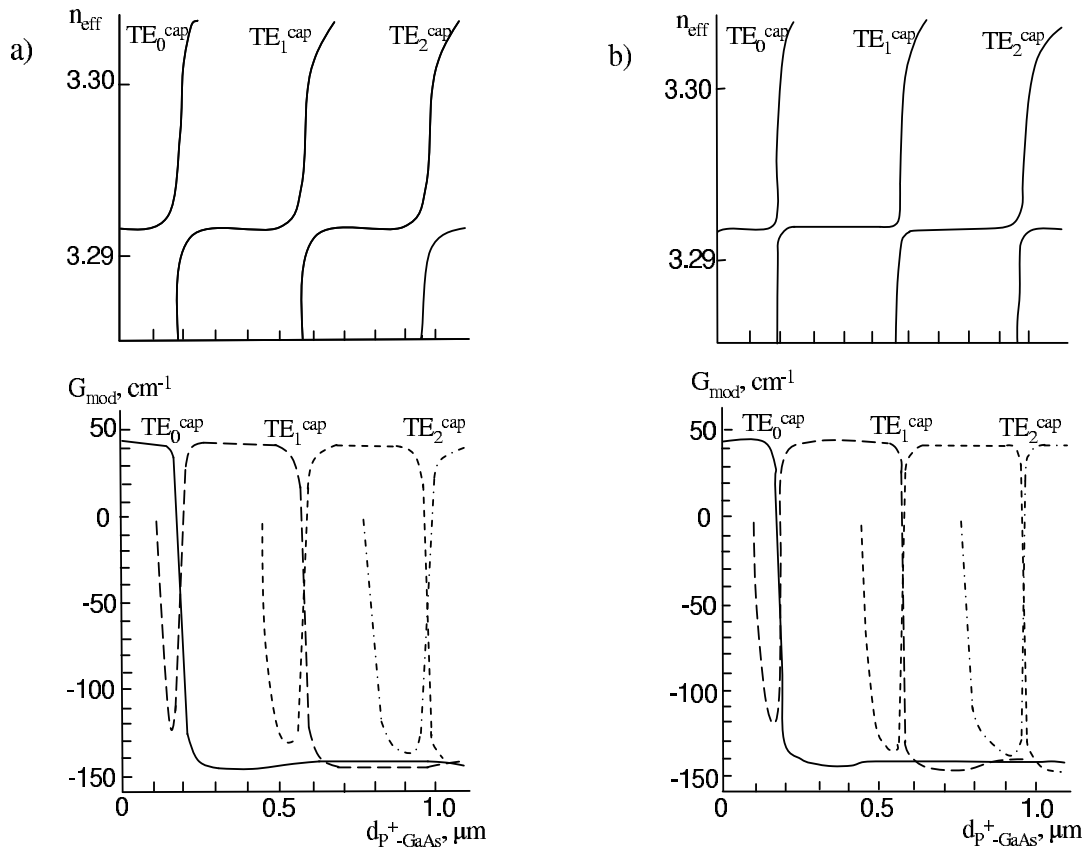


Figure 2.8 Effective index, n_{eff} , and modal gain, G_{mod} , plots versus cap layer thickness, d for two cladding layer thicknesses of (a) $0.6 \mu m$ and (b) $0.8 \mu m$. Resonance points shown where two TE mode branches of n_{eff} plots come close to intersecting. [14]

variation in the laser mode gain. The spacing of spectral peaks corresponds to different thicknesses of the substrate rather than to the cavity length of the active region. Again, as with the cap layer, if the mode coupling is very strong, lasing action will cease. From this discussion, it is seen that ghost mode coupling must be taken into account when designing semiconductor laser structures. Structures that have higher optical leakage, *i.e.*, thinner cladding layers, are more vulnerable to this loss mechanism. Optical leakage grows exponentially as the cladding layers become thinner. [14]

To investigate the modal development processes and ideas laid out in this chapter, descriptions of experiments devised to do so are presented next. This includes descriptions of the photoluminescence and laser experiments and the time resolved photoluminescence experiment.

III. Experiment

Laser emission from an optically pumped mid-IR semiconductor device results from the recombination of electron-hole pairs as described previously. This radiative emission takes place several nanoseconds after the initial excitation. To investigate this process and the subsequent lasing events that occur, the incorporation of a lasing technique into a time-resolved photoluminescence (TRPL) experiment is attempted. The TRPL experiment uses an upconversion technique developed by Mahr and Hirsch [25] to resolve sub-picosecond occurrences over a 3-ns time period. This technique does so by mixing the short pulses of a source laser beam with the longer photoluminescence (PL) pulses of the semiconductor sample being investigated inside a nonlinear crystal. This “light-gate” allows the PL signal to be mapped out temporally by simply adjusting (delaying) the arrival time of the short laser pulse as shown in Figure 3.1 [33]. To incorporate laser devices into this experiment, two other tasks must be performed before TRPL takes place. The first is to characterize the semiconductor samples for their peak wavelengths using photoluminescence. The second task is to develop a technique to stimulate the samples into lasing by redirecting and reshaping the source beam, processing the samples, and modifying other equipment. Since the overall experimental setup is designed for TRPL, this chapter will first discuss upconversion theory. This will be followed by a description of the setup, which includes the photoluminescence and lasing modifications.

3.1 Upconversion Theory

Upconversion is the process of generating a beam of light of one wavelength from two or more beams of differing wavelengths within a nonlinear crystal. This process is known as sum frequency generation (SFG). For a medium to be nonlinear, its polarization density should be such that it can be expressed as a Taylor series expansion:

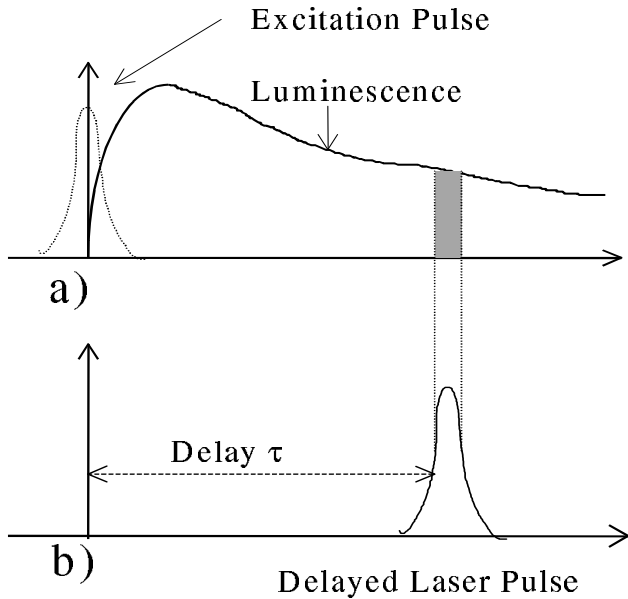


Figure 3.1 Wave mixing resulting in the time resolution of the luminescence. (a) Depicts the luminescence curve over time. (b) Represents the pump beam at some delay time τ . [18]

$$P_i = \varepsilon \chi_{ij} E_j + 2\varepsilon \chi_{ijk} E_i E_j + \dots, \quad (3.1)$$

where P is the polarization density, E is the incident electric field, ε is the permeability of free space, and χ is the susceptibility [41]. The nonlinear crystal used for this experiment is KTiOAsO₄ (KTA) which has second-order and higher nonlinearity in the Taylor expansion term. Since the higher order terms add little significance to the overall output, they are neglected. It is found that optical beams treated as plane waves require two conditions be met as a result of the second order term. The first is frequency matching, where the pump beam frequency and laser signal frequency sum to the frequency of the upconverted beam such that

$$\omega_3 = \omega_1 + \omega_2. \quad (3.2)$$

This expression can be cast in terms of wavelength to give

$$\frac{1}{\lambda_{up}} = \frac{1}{\lambda_{Laser}} + \frac{1}{\lambda_{Pump}} \quad (3.3)$$

where λ_{Laser} is the signal wavelength, λ_{Pump} is the pump wavelength, and λ_{up} is the upconverted wavelength. This equation expresses the conservation of energy required to produce upconversion.

The second condition is phase matching:

$$\vec{k}_{up} = \vec{k}_{Laser} + \vec{k}_{Pump} \quad (3.4)$$

where each \vec{k} is one of the wavevectors ($|k| = 2\pi n/\lambda$) shown in Figure 3.2. These vectors are the corresponding wavevectors to the wavelengths in equation 3.3. Applying the law of cosines to equation 3.4 and replacing \vec{k} gives

$$\frac{n_{up}^2}{\lambda_{up}} = \frac{n_{Laser}^2}{\lambda_{Laser}} + \frac{n_{Pump}^2}{\lambda_{Pump}} - 2 \frac{n_{up} n_{Laser}}{\lambda_{up} \lambda_{Laser}} \cos(\pi - \gamma), \quad (3.5)$$

where n_{up} , n_{Laser} , and n_{Pump} are the indices of refraction for each beam and γ is the angle between the laser and pump wave vectors.

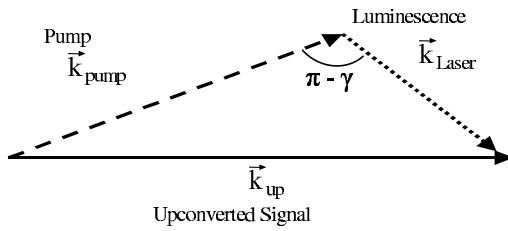


Figure 3.2 Upconverted signal in terms of wavevectors [18].

The indices of refraction for a nonlinear medium vary according to the polarization of the incoming light and depend upon the incident wavelength and angle of incidence. For KTA, the indices can be expressed in terms of the three principal axis n_x , n_y , and n_z as functions of wavelengths. The crystal is cut at an angle $\Phi = 43^\circ$

between the crystal axis and the normal to the crystal surface in the X-Z plane. Therefore, according to the Sellmeier equations [16]:

$$n_o(\lambda) = n_y(\lambda) \quad (3.6)$$

$$n_e(\lambda) = \frac{n_x(\lambda)n_y(\lambda)}{\sqrt{n_z(\lambda)^2 \cos(\theta)^2 + n_x(\lambda)^2 \sin(\theta)^2}} \quad (3.7)$$

where n_o and n_e are the ordinary and extraordinary indices of refractions, respectively, θ is the angle between the extraordinary beam and the z axis, and λ is the wavelength of the incident light. In the TRPL experiment, the leg used to excite the sample is ordinarily polarized while the mixing leg is extraordinarily polarized. The KTA crystal properties cause the resulting upconverted signal to be ordinarily polarized. This equation is solved for θ given a wavelength and can be changed by rotating the crystal. To meet the phase matching condition for a given experimental setup, a MathCad program with these equations is used (see appendix A) to calculate the necessary crystal tilt angle. The experimental setup is described in the subsequent section explaining how the two legs are mixed and how the upconverted beam is collected.

3.2 Experimental Setup

3.2.1 Laser Source. The experiment starts with a Coherent Mira 900 mode-locked Ti:Sapphire laser used as a source beam. This source operates at 1.9 Watts average power with a repetition rate of 76 MHz and peak wavelength of 810 nm. The repetition rate corresponds to a sample excitation every 13.2 ns, providing time to examine the luminescence decay. This laser produces pulses that are 130 fs wide, which is essential to achieving the level of resolution required by this experiment. The Ti:Sapphire beam is optically pumped by a Coherent Innova argon-ion (Ar^+) laser operating at 10.8 Watts.

Two methods are used to measure the pulse width of the Ti:Sapphire laser and verify the results. First, an INRAD Model 5-14BX Autocorrelator is used. The autocorrelator produces highly accurate measurement results almost instantaneously using a computer. In a method analogous to the experiment, the autocorrelator splits the Ti:Sapphire laser beam into two paths and focuses them into a non-linear crystal (LiIO_3) where they mix, effectively mixing the Ti:Sapphire beam with itself. This phenomenon is known as second harmonic generation (SHG) and produces a beam of light at half the wavelength of the original. This frequency-doubled beam is collected by an appropriate detector and sent to a computer for analysis. The autocorrelation function is accomplished by varying the path length of one of the beams of incoming laser radiation. This action performs a convolution of the two identical beams producing a temporal response. Measuring this response at the full width at half maximum (FWHM) point, the pulse width is determined, which is related to the width of the laser pulse in time.

To verify the autocorrelator results, the experimental setup is used in exactly the same fashion by replacing the KTA crystal with a LiIO_3 crystal and focusing the laser source leg on the cryogenic mount inside the vacuum chamber instead of on a semiconductor sample (reference Figure 3.3). By varying the pump leg and recording the output signal collected by a spectrometer fitted with a photo-multiplier tube (PMT), a similar response is mapped. The two methods are correlated by multiplying the response of the experiment by 0.648, which results from fitting a sech^2 function to the lineshape of the autocorrelator result. This is done on suggestion of the manufacturer. The temporal and spectral plots of the Ti:Sapphire source are shown in Figure 3.4.

To produce both second harmonic generation and sum frequency generation (upconversion), the focused signal beam and pump beam must overlap inside the nonlinear crystal (see Figure 3.3). Knowledge of the focused spot size of these path length legs is thereby necessary to ensure overlap. Thus, the cross section profile of

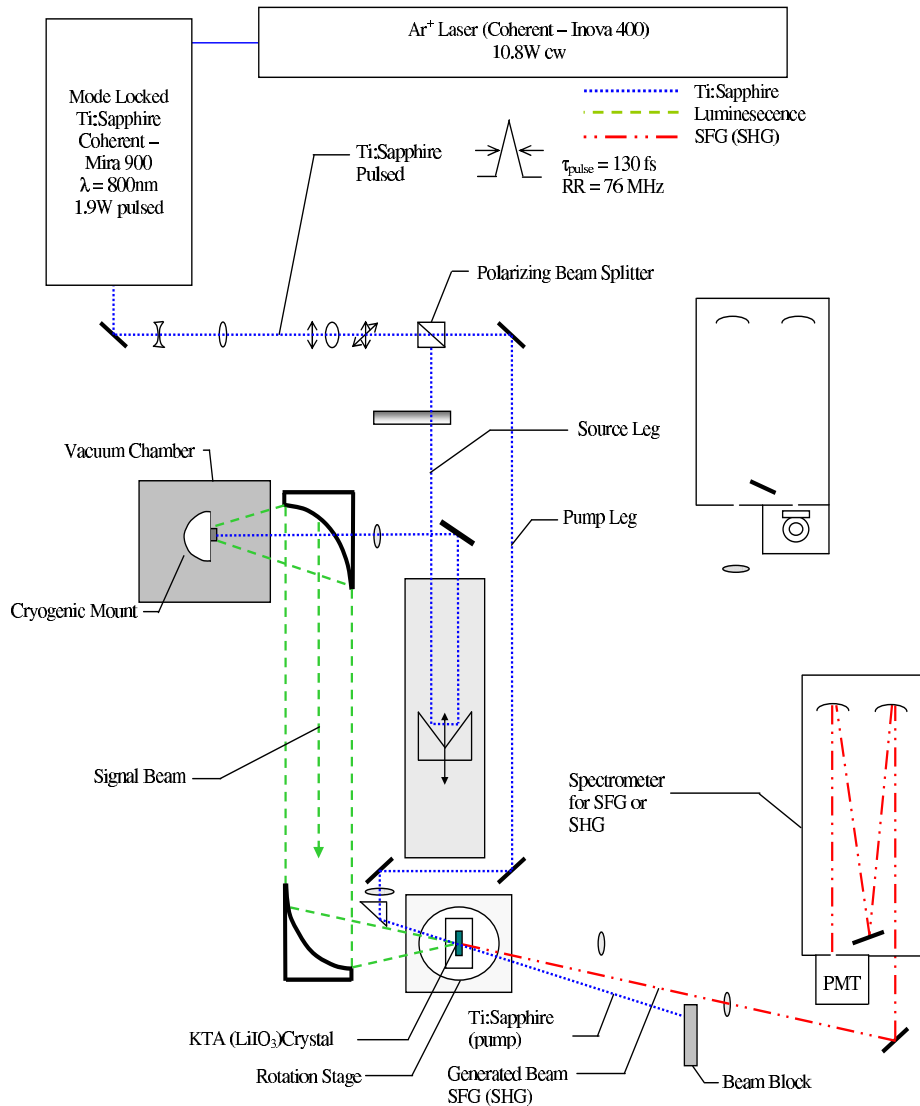


Figure 3.3 Schematic of experimental setup showing the cryogenic mount, source leg, pump leg, and signal beam [12].

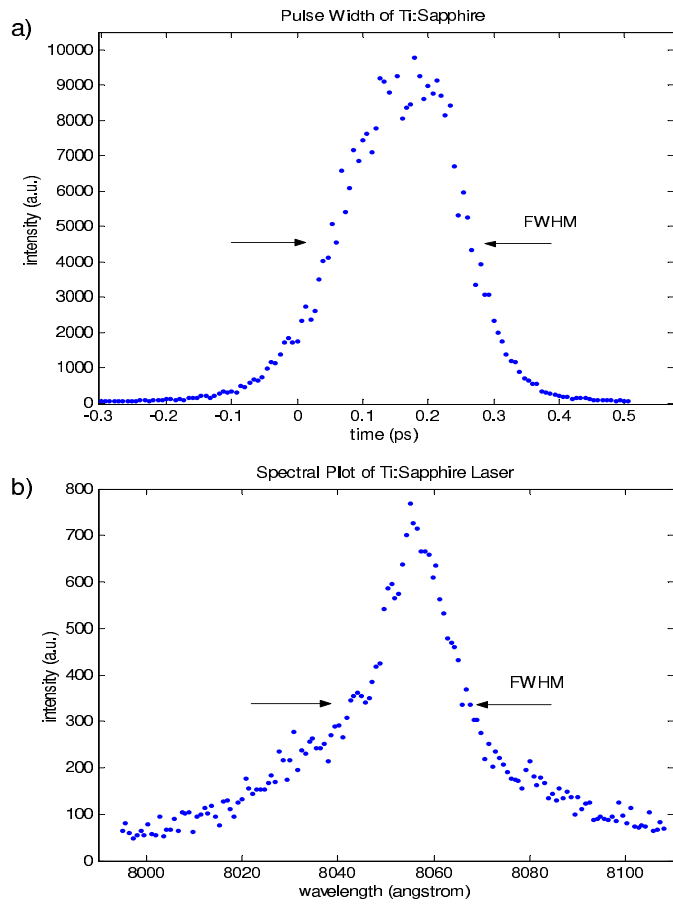


Figure 3.4 (a) Pulse width of Ti:Sapphire laser. FWHM is measured to be $\Delta t_m = 207$ fs. The actual pulse width is $\Delta t_a = 134$ fs after multiplying by the correction factor 0.648. (b) Spectral width of Ti:Sapphire pulse of 2.5 nm.

the Ti:Sapphire laser must be measured in order to calculate the focused spot sizes of the two legs. A Coherent-Mode Master was used to measure the M^2 value and beam cross section along the x- and y- directions. The M^2 value is a measure of how closely the actual beam represents a perfect Gaussian beam. Measurements were taken at three different positions and averaged to give a final measurement. The diameter in the x-direction was 6.918 ± 0.0623 mm and in the y-direction was 5.926 ± 0.0846 mm. The radial value of this elliptical shape was 6.442 ± 0.0119 mm [11]. The lens used to focus the pump beam into the nonlinear crystal has a focal length

of 200 mm while the lens used to focus the source beam onto the sample has an effective focal length of 300 mm. The focal point spot sizes are calculated using the following equation for a Gaussian beam [11]:

$$2w = \frac{4}{\pi} \cdot \frac{\lambda f}{D} \quad (3.8)$$

where $2w$ is the focused beam diameter in the assigned direction, f is the focal length, and D is the beam diameter entering the lens (values given above). The calculations for the spot sizes for the two lenses are given in the Table 3.1.

Table 3.1 Calculated spot sizes of 200 mm and 300 mm lenses in the x, y, and radial directions.

	x (μm)	y (μm)	R (μm)
Pump Beam (200 mm)	29.7 ± 0.27	34.78 ± 0.50	31.99 ± 0.06
Laser Signal Beam (300 mm)	44.68 ± 0.40	52.17 ± 0.74	47.99 ± 0.09

For the Ti:Sapphire laser, the M^2 values are 1.20, 1.36, and 1.387 for the x, y, and radial directions, respectively. This means that the Ti:Sapphire has a waist that is 1.20 times the diffraction limited Gaussian beam waist in the x-direction, 1.36 times in the y-direction, and so on. [11]

3.2.2 Beam Paths. The beam leaving the Ti:Sapphire travels through a series of optics before being split into its two respective paths: the source beam path and the pump beam path. The beam is first expanded and collimated. It then travels through a half-wave plate, allowing the power division in each leg to be adjusted. Next, wavelengths below 700 nm are filtered out (reference Figure 3.5). Finally, the beam passes through the beamsplitter, where it is divided into horizontal and vertical polarizations.

3.2.2.1 Signal Beam Path. The signal path contains the laser source beam, which is the semiconductor sample's optical pump, and the emission signal, or the semiconductor's luminescent emission. The source beam leaves the beam-splitter vertically polarized, passes through a neutral density filter, and proceeds on to a gold-coated retroreflector mounted on a moveable stage. Before reaching this stage, the beam passes through a chopper wheel spinning at 200 MHz when taking photoluminescence or laser spectra. Otherwise, the chopper is off allowing the beam to pass unimpeded. From the delay stage, the beam is directed to enter the vacuum chamber containing the semiconductor samples in one of three configurations.

1. Photoluminescence Configuration. This configuration is the standard setup for the signal beam path when used for upconversion and photoluminescence. From the delay stage, the source beam is directed into the vacuum chamber containing the semiconductor sample by a 300-mm focal length lens. This lens focuses the beam to a point at the surface of the sample, which is mounted on the flat side of a cryogenic cold finger inside the chamber (reference Figure 3.5). The luminescence of the sample is collected by a gold-coated, off-axis parabolic mirror. This mirror directs the luminescence to an identical mirror, which focuses it to the location where a nonlinear crystal will be positioned when used for upconversion. Each parabolic mirror has a focal length of 150 mm enabling the pair to act as a one-to-one imaging system, with the sample in the object plane and the crystal in the image plane. From the nonlinear crystal location, the signal is collected by a CaF₂ lens, which passes light in the IR spectrum, thereby re-collimating it. A second CaF₂ lens focuses the signal on the entrance slit of a 1/2-meter SPEX spectrometer with a 4-μm-blazed grating. The grating has 300 grooves/mm with a calculated resolution of $6.67 \times 10^{-6}W$ where W is the slit width of the spectrometer in millimeters. A Standard Research Lock-in Amplifier amplifies the signal from a InSb detector, sending it to a computer for analysis. The amplifier is synchronized to the

chopper wheel for phase-locked detection. Luminescence spectra were taken for the five samples under investigation at a pump power of 300 mW and a temperature of 77 degrees Kelvin. The results are shown Chapter V.

2. Laser Configuration. In this configuration, the beam coming from the delay stage is directed to enter the cryostat from the side (see Figure 3.6). The beam is focused onto the semiconductor sample using a two-lens system to shape the beam into a narrow, horizontal stripe across the cleaved facets of the sample under investigation. The first lens is 400-mm bi-convex, which initially focuses the beam. It is placed such that the beam passes through a focus and diverges into a spot size at the sample of 2 mm, which is the size of the largest laser cavity. The beam then passes through a cylindrical lens, focusing it in the vertical direction down to the horizontal stripe (refer to Figure 3.6). The Beam Code beam profiling system was used to make measurements of the stripe to ensure the proper shape at the location of the semiconductor sample. Figure 3.7 shows the profile of the beam in the x- and y- directions. It is measured to be 2.05-mm wide at the $1/e^2$ points of the Gaussian beam. The horizontal stripe is positioned to be perpendicular to the cleaved facets of the semiconductor sample resulting in the formation of a gain-guided optical waveguide along this direction. This waveguide forms the laser cavity of the sample enabling laser emission.

This configuration required the mounting surface of the cold finger to be positioned at an angle slightly off normal to the entering beam. This enables the laser emission generated at the sample's edge to be collected by the off-axis parabolic mirror, 90° from the source beam. The laser emission is directed as before to a focus at the location of the nonlinear crystal. When looking for laser emission, the crystal is removed allowing the emission to travel down the PL path described in part 1 where it is sent into the spectrometer and subsequent

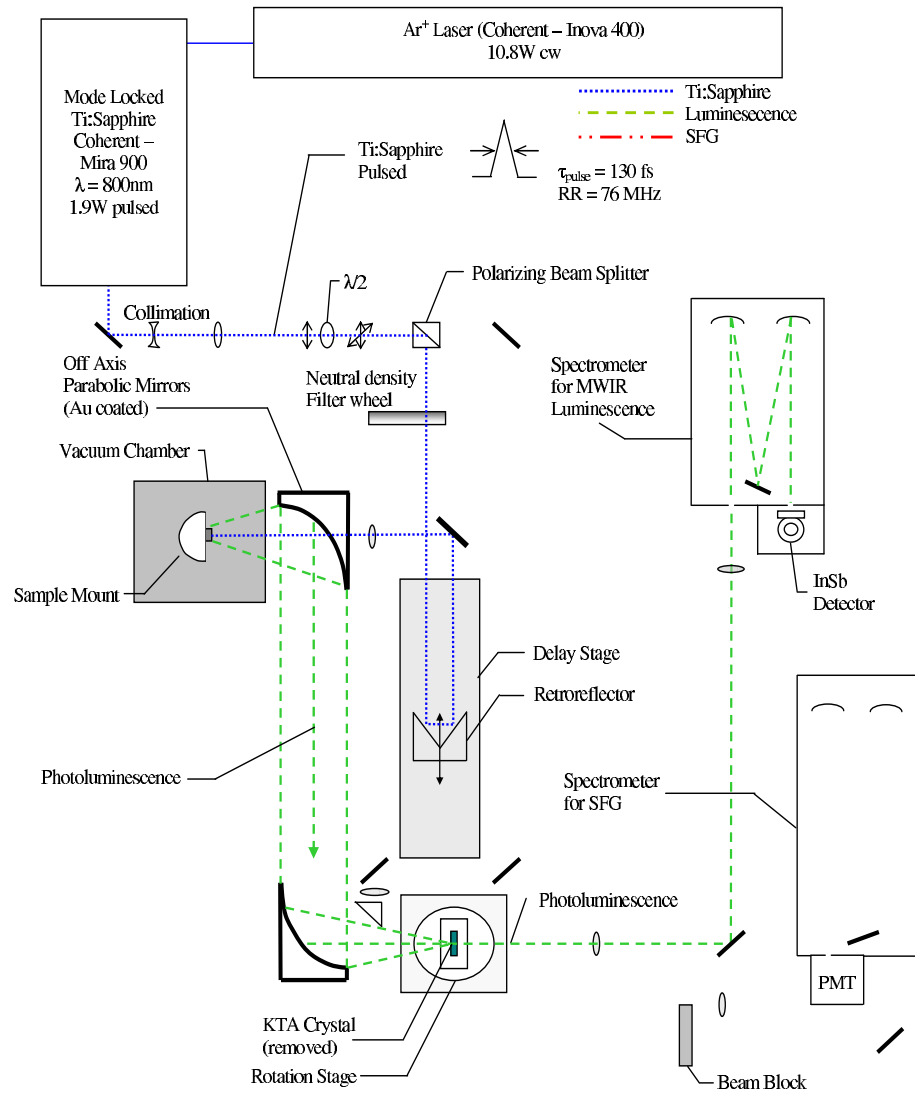


Figure 3.5 Photoluminescence configuration. The flat surface of the sample mount is positioned normal to the off-axis, parabolic mirror. The photoluminescence generated is collected by a series of CaF_2 lenses and sent to a spectrometer for evaluation. [12]

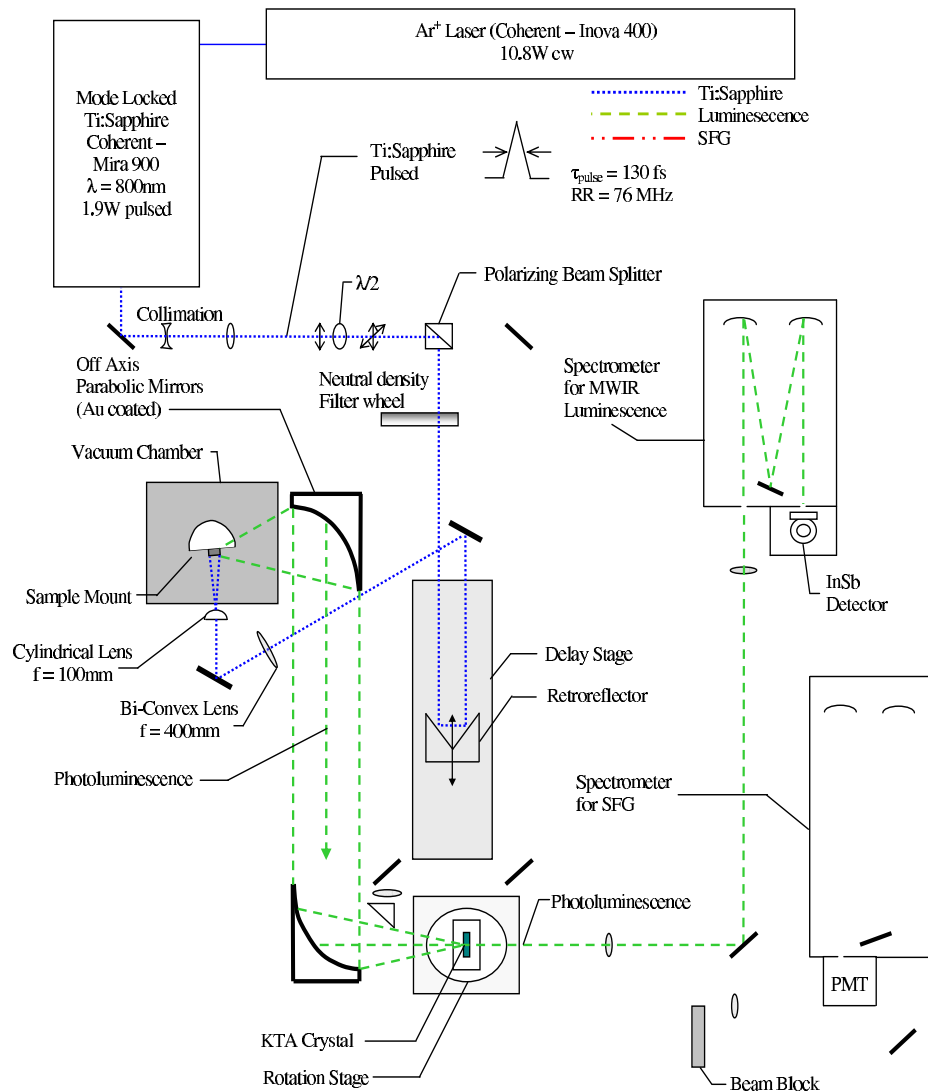


Figure 3.6 Laser configuration. The laser source beam is directed into the cryostat from the side, passing through a 200 mm biconvex lens and a 100 mm cylindrical lens forming a horizontal stripe. The surface normal of the cold finger is positioned at a slight angle to the incoming beam.

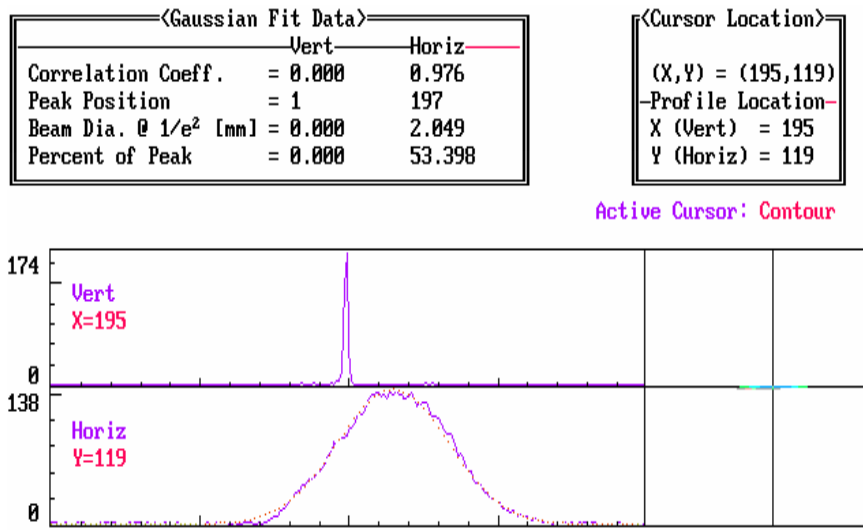


Figure 3.7 Laser source focused to a horizontal stripe. Profile along x axis shows a beam diameter at the $1/e^2$ point of 2.049 mm.

detector. In this way, spectra can be taken over the luminescence wavelengths of the samples to look for lasing modes.

3. Luminescence Upconversion Configuration. This configuration is the standard setup used for upconversion when using the luminescence of the semiconductor sample. From the second parabolic mirror, the beam is focused into the nonlinear crystal mounted on a rotation stage, where it mixes with the pump beam described in the next section. When conducting the TRPL experiment, the path length of the source-signal leg becomes important as it must be comparable to the pump beam path. Using the delay stage encountered earlier in the source path (Figure 3.8), this leg can be adjusted so that luminescent emission can be mapped (described previously). Using a second, two-dimensional retro-reflector at the top of the stage, the optical path length of the beam can vary by 4 ns in time. The combination of the two retro-reflectors causes the beam to pass through the delay stage twice, or a total of 120 cm. Dividing this length by the speed of light gives this 4 ns variance.

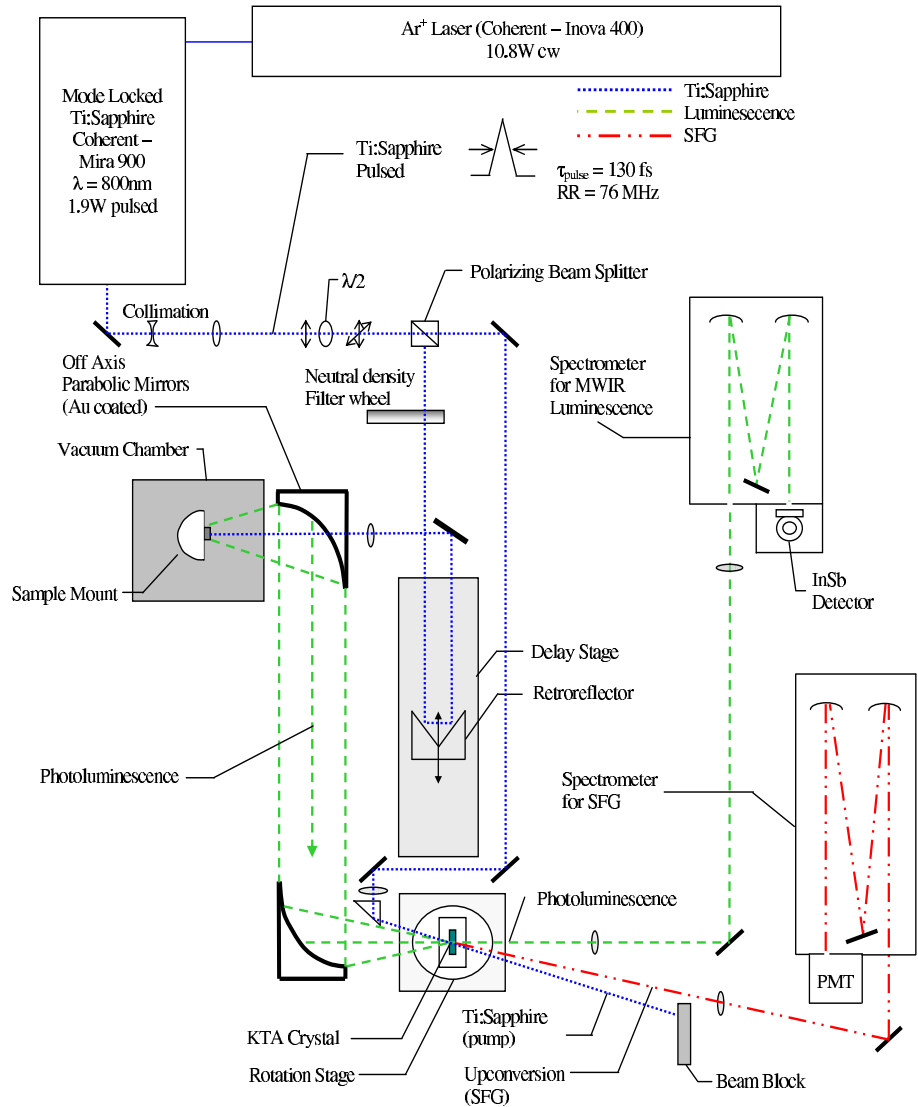


Figure 3.8 Experimental set up in the TRPL experiment. The Ti:Sapphire laser creates a 130 fs pulse that is split into two paths. The laser signal beam travels through a delay stage before exciting the sample. Luminescence is collected and mixed with the pump beam in the KTA crystal. The upconverted beam is then directed to the spectrometer and photon counter. [12]

3.2.2.2 Pump Beam Path. The pump beam is horizontally polarized when it leaves the beamsplitter. As mentioned previously, it travels an optical distance similar to the source-signal beam path. A 200-mm focal length lens is used to focus the beam to a spot within the nonlinear crystal, shown in the schematic (Figure 3.8). A prism is used to redirect the beam into the crystal at an angle of 20° with respect to the signal beam. This angle is used in equation 3.5 to find the tilt angle of the crystal required for upconversion. At this angle, the pump beam mixes with the signal beam to create the upconverted signal.

3.2.2.3 Beam Collection and Overlap. To produce the upconverted beam, the two signal paths must overlap in time and space within the nonlinear crystal such that the two optical waves interact with one another according to the phase matching and frequency matching conditions (equations 3.2 and 3.4). To align the two beams in space, a 25- μm pinhole is placed at the position of the nonlinear crystal and the two beams are focused through it. The size of the pinhole ensures sufficient beam overlap as both beam spot sizes are larger in both x and y directions, requiring that they exist at the same position in space to pass through the pinhole.

Once the beams are aligned as such, the retroreflector delay stage must be adjusted so that both beams are aligned in time. To do this, the LiIO₃ crystal is mounted as the nonlinear crystal and the delay stage is incrementally positioned until the SHG signal occurs (reference Section 3.2.1). This signal is in the visible spectrum so that it is easily seen when the the two paths are overlapping in time. With this, alignment in time and space is confirmed.

The upconverted beam is collected by a 400-mm focal-length lens which focuses the beam to the slits of a 3/4-meter SPEX spectrometer. Before reaching the spectrometer, it passes through an 800-nm filter to remove residual Ti:Sapphire wavelengths, and through a periscope to bring it to the proper level of the slits. The spectrometer grating has 1200 grooves/mm which gives a resolution of 3.3 nm at a

slit width of 3 mm. The signal is then collected by a GaAs PMT chilled to 0°C and biased at 2000 V. The PMT converts the signal into an electrical signal which is amplified and sent to a Standard Research SR400 photon counter which interfaces with a computer to control the experiment. The spectrometer grating or the delay stage can be incremented while taking photon counts.

With these descriptions of the experimental arrangements set forth, the samples being investigated are presented in the next chapter. This chapter includes the material makeup and structural design of the five samples followed by the preparation of each for input into the experiment.

IV. Samples and Sample Preparation

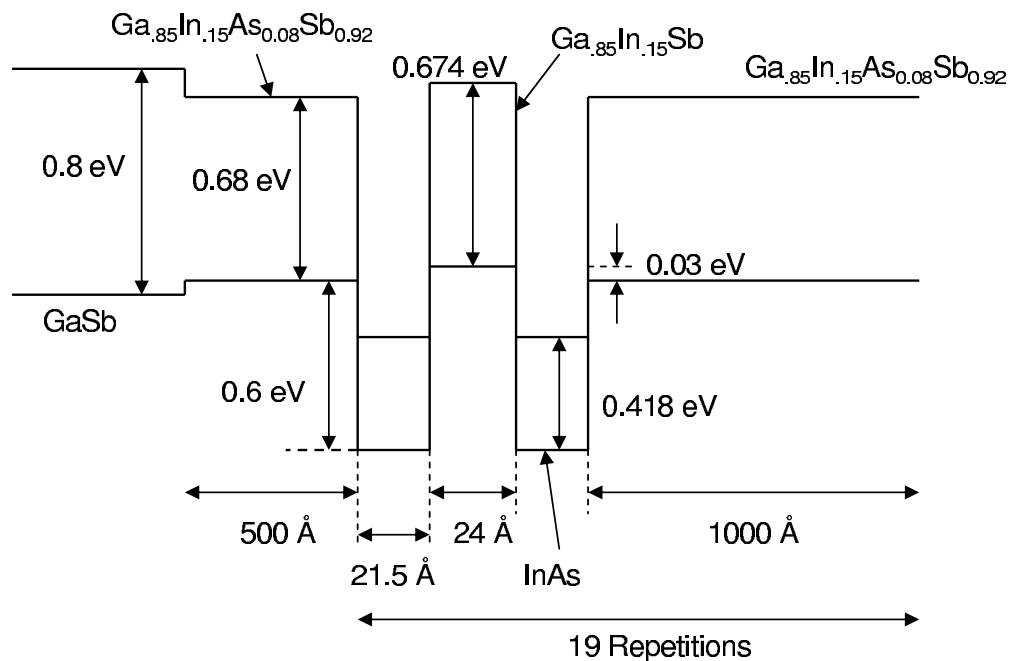
Five different samples were investigated in this experiment. Samples 201-056 and B were provided by Lincoln Laboratory at the Massachusetts Institute of Technology (MIT). Samples R0-62, R1-73, and R2-43 were provided by the Directed Energy Directorate of the Air Force Research Lab at Kirtland Air Force Base, New Mexico (AFRL/DE). Each was investigated using the experiments described above in an attempt to achieve laser emission to characterize modal behavior. [23, 35]

4.1 Sample Description

The samples are divided into categories based on their type and waveguiding ability. The type defines the conduction band and valence band energy profiles. In a type-I structure, the quantum wells formed in the two bands are spatially aligned meaning the electrons and holes will be confined in the same material layer of the device. In a type-II structure, the wells are offset, with the electrons confined in one material layer and the holes confined in the adjacent material layers (reference Figure 2.2). Only sample B is a type-I structure while the rest are type II.

The two types of light-guiding used are tight and dilute waveguides. A tight waveguide makes use of cladding layers as described in Section 2.2. This confines the TEM optical modes to the active region of the device with minimal leakage into the outer layers. Dilute waveguides use only the GaSb cap and substrate layers for confinement which allows evanescent leakage of the TEM modes into them. Samples B and R0-62 are tight waveguide structures and samples 201-056, R1-73, and R2-43 are dilute waveguide structures. The structural makeup of the samples are shown using diagrams in Figures 4.1 through 4.4. A schematic of the waveguide types is shown in Figure 4.5.

Energy

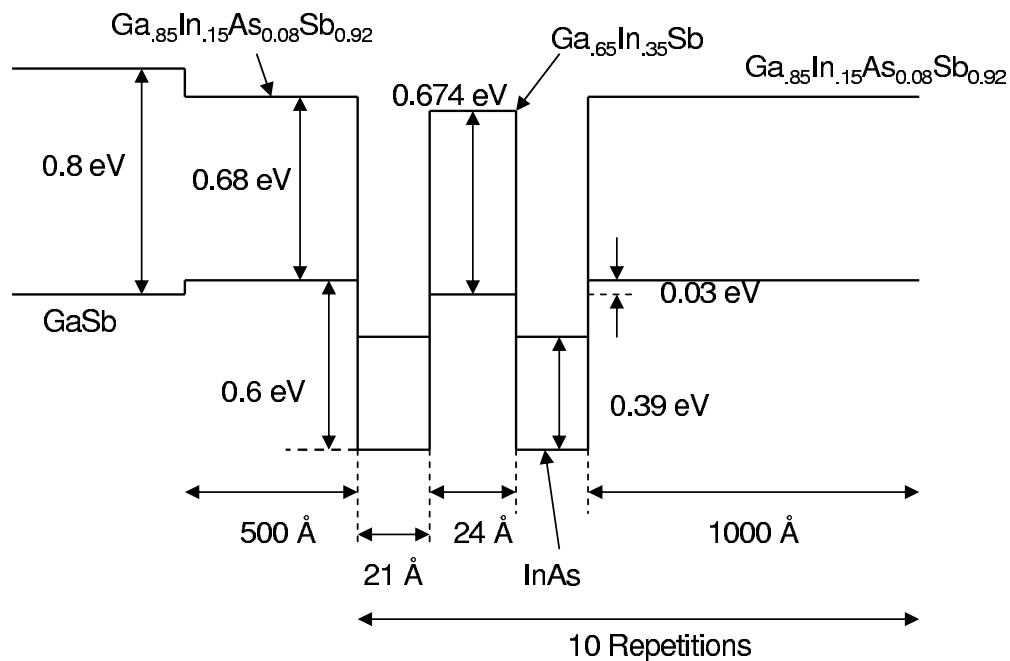


Refractive Index

$$n = 3.82 \quad n_{\text{eff}} = 3.88 \text{ (effective index of active region)}$$

Figure 4.1 Sample 201-056 energy band and refractive index diagram drawn to scale. This sample is a type-II, dilute waveguide structure. [18, 27, 35, 38]

Energy



Refractive Index

$$n = 3.82 \quad n_{\text{eff}} = 3.88 \text{ (effective index of active region)}$$

Figure 4.2 Energy band and refractive index diagram for samples R1-73 and R2-43 drawn to scale. These samples are type-II, dilute waveguide structures. [17,23,27,38]

Energy

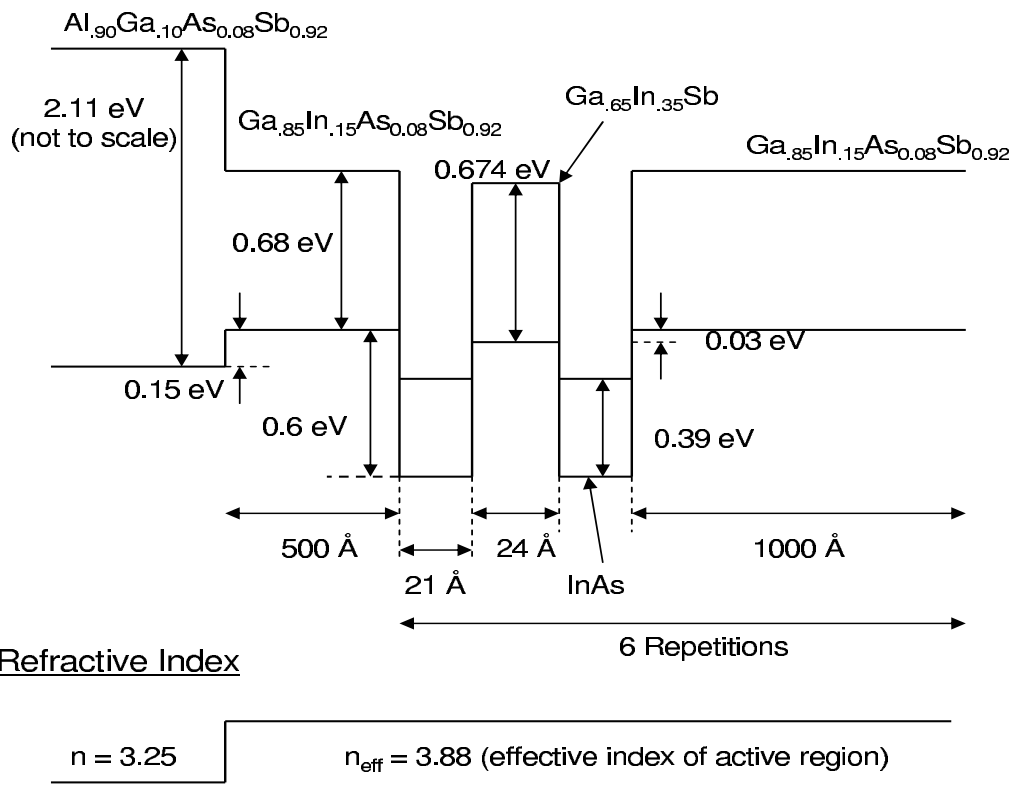
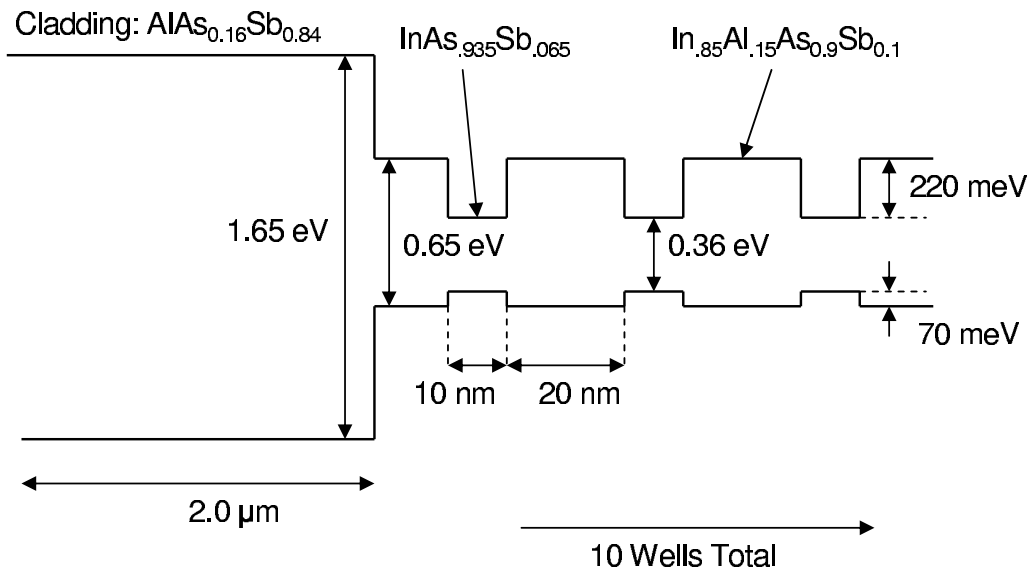


Figure 4.3 Sample R0-62 energy band and refractive index diagram drawn to scale. This sample is a type-II, tight waveguide structure. [17, 23, 29, 38]

Energy



Refractive Index

$$n = 3.17$$

$$n_{\text{eff}} = 3.87 \text{ (effective index of active region)}$$

Figure 4.4 Sample B energy band and refractive index diagram drawn to scale. This sample is a type-I, tight waveguide structure. [12, 35]

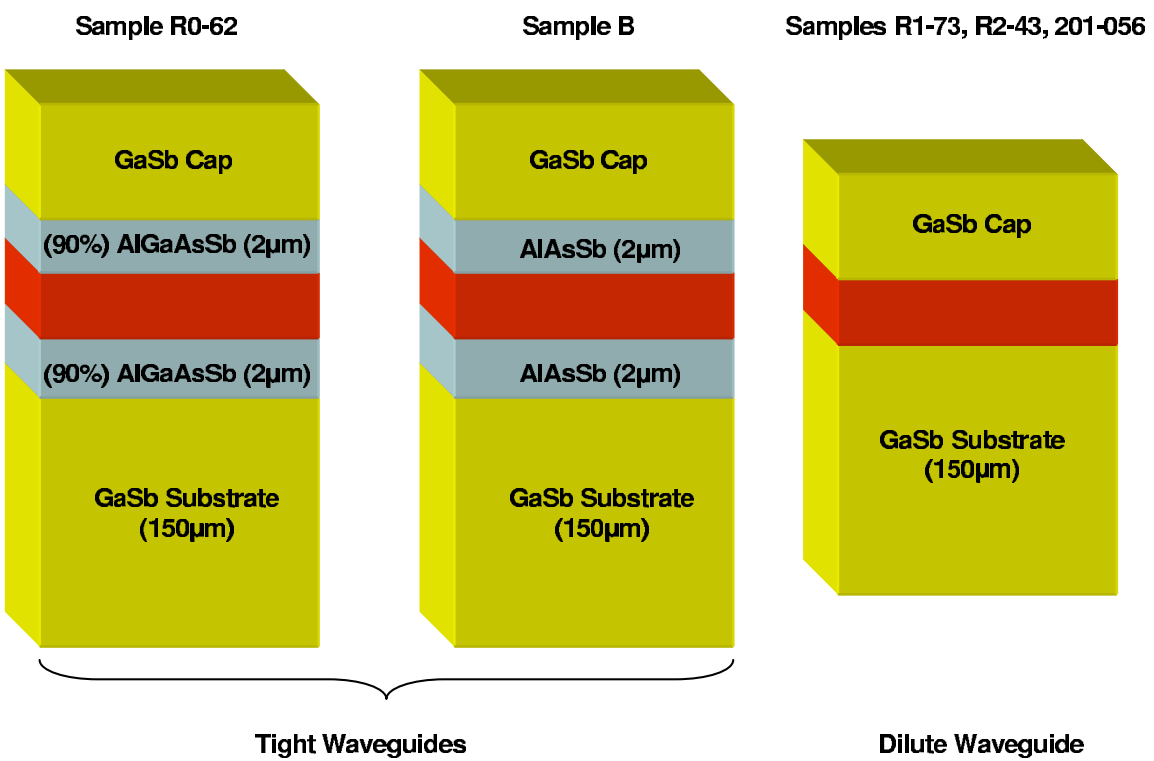


Figure 4.5 Tight waveguides having cladding layers shown in gray and dilute waveguide having no cladding layers.

4.2 Sample Preparation - Etching

The three structures provided by AFRL/DE require an optical pump emitting at wavelengths larger than $1.709\text{ }\mu\text{m}$ to penetrate through the GaSb cap layer into the active region. In order to make these samples compatible with the experiments presented, the cap layers of the samples were etched to a depth which allowed wavelengths of 800 nm to penetrate into the active region. According to the condition for absorption in a semiconductor, the small signal gain is related to the thickness of a semiconductor layer by

$$G = \exp(\gamma d) \quad (4.1)$$

where G is the small signal gain, γ is the gain coefficient and d is the layer thickness [37]. When loss occurs, γ becomes $-\alpha$ representing loss in the material. For GaSb at $\lambda = 800\text{ nm}$, $\alpha = 4 \times 10^4\text{ cm}^{-1}$, where, for 50% absorption, the thickness of the cap layers must be 173.3 nm or less. With this in mind, the three samples were etched to remove as much of the cap layers as possible while retaining optical confinement. The cap layer of sample R0-62 was completely etched off because the structure retains cladding layers to confine the optical lasing modes. Samples R1-73 and R2-43 were etched to a depth of $3.984\text{ }\mu\text{m}$ leaving only 16 nm of the cap layer. Using equation 4.1, this translates to a loss of only 6.2% of the Ti:Sapphire pump.

Etching of the GaSb cap layers was carried out in collaboration with the Aerospace Components Division of the Sensors Directorate, Air Force Research Lab, Wright-Patterson Air Force Base, Ohio (AFRL/SND) by first etching a piece of GaSb bulk material to determine the etch rate of the reactive ion etch (RIE) used. The process is as follows:

1. The sample is cleaned by placing it in a spindle device rotating at 500 rpm.
The sample is rinsed in the following solutions while spinning:
 - (a) Acetone - 30 seconds

- (b) Isopropyl Alcohol - 30 seconds
 - (c) Distilled water - 30 seconds
2. Photoresist (Shipley #1813) was applied in two spots followed by a 5 minute bake on a hot plate (reference Figure 4.6)

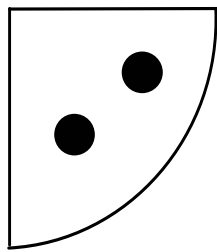


Figure 4.6 Shape of GaSb test piece used for etch study with approximate locations of 1813 photoresist.

- 3. The sample undergoes a plasma ash for 4 minutes with an oxygen flow rate of 200 standard cubic cm (sccm) at 200 watts of RF power.
- 4. The sample was placed in the reactive ion etch for 5 minutes
- 5. Once the etching was complete, the resist was removed and measurements of the etch depth were taken using a profilimeter.

The depth of the etch was determined to be $24.9 \mu\text{m}$, giving an etch rate of $4.98 \mu/\text{min}$. This rate was used to attain the etching depths given above.

4.3 Sample Preparation - Cleaving

In addition to providing sufficient optical stimulation via the source beam, a resonant cavity is needed to produce stimulated emission. As discussed in Section 2.3, this cavity is formed when the photon-producing medium is placed between two

perfectly parallel reflecting surfaces. For the samples here, the reflecting surfaces are created by cleaving the samples along two parallel crystal planes. This action produces perfectly parallel facets that are highly reflective. When the source beam stripe is applied perpendicular to these surfaces, an optical waveguide is formed confining photons to the focused stripe area. Under optimal conditions, resonance takes place and lasing occurs. The separation between these facets is known as the cavity length. This length is used in determining the settings of the detection spectrometer and dictates the resolution needed to see the longitudinal lasing modes. Using equation 2.13 and the relation $\lambda = c/\nu$, an equation for the wavelength spacing of the modes is given by

$$\Delta\lambda = \frac{\lambda^2}{2nd} \quad (4.2)$$

where λ is the peak wavelength, n is the index of refraction of the active region, and d is the cavity length [37]. Using this equation with that for the wavelength resolution of the spectrometer

$$\Delta\lambda = \frac{aw}{fm} \quad (4.3)$$

the required slit width settings of the spectrometer can be determined. In this equation, a is the groove spacing of the spectrometer diffraction grating, w is the spectrometer slit width, f is the spectrometer focal length, and m is the order of spectra reflected by the grating [26]. The cavity lengths for samples R0-62, R1-73, and R2-43 are 2 mm, sample 201-056 is 1.5 mm and sample B is 1mm. The results of experimentation using the theory and settings discussed up to this point are presented in the next chapter.

V. Results and Analysis

In this chapter, the results of the experimentation discussed in Chapter III are presented. First, the results of the computer models generated for the three different laser structures are presented. Next, the results of the PL data and lasing data are given. Finally, the results of the upconversion experiment and setup are shown.

5.1 Modelling Results

The results of models produced by Mike Tilton of AFRL/DE showing the mode development in the etched waveguides are given in Figures 5.1 and 5.2 [23]. These models predict only the development of ghost modes and indicate that the main lasing modes in the active region cannot be supported. Only the two lowest loss modes are shown having approximately the same gain. Furthermore, Tilton suggests that any lasing that does occur through these ghost modes will not be detectable.

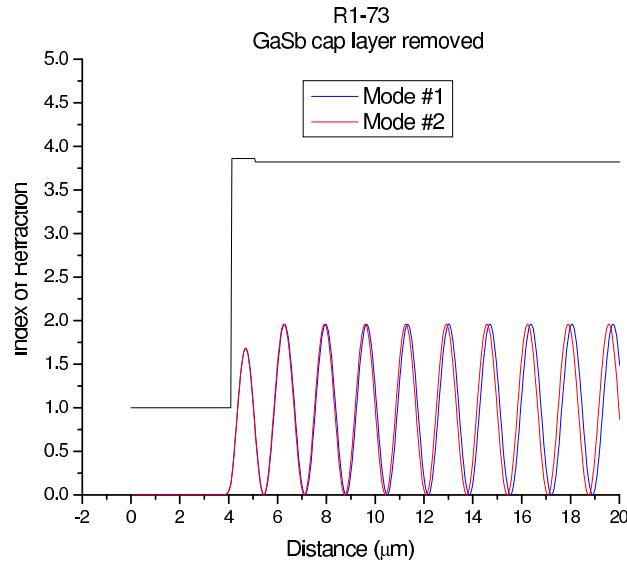


Figure 5.1 Model of TE modes in sample R1-73. Only ghost modes are predicted as shown by the two lowest loss modes. [23]

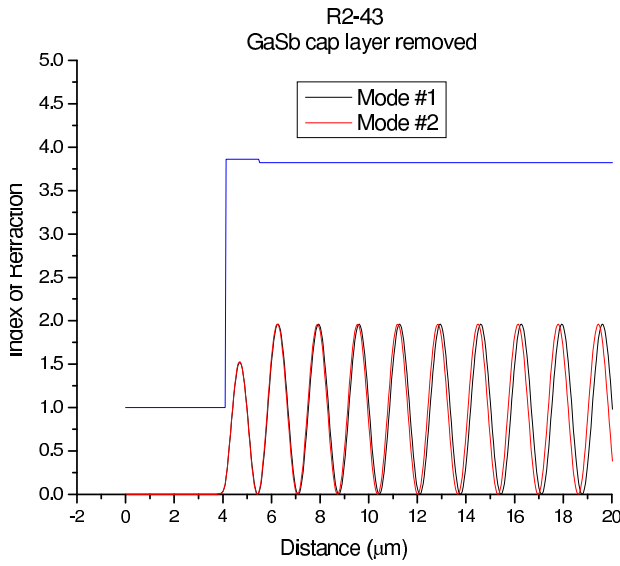


Figure 5.2 Model of TE modes in sample R2-43. Again, only ghost modes are predicted as shown by the two lowest loss modes. [23]

5.2 PL Results

With the experimental setup configured to take photoluminescence spectra as described in Part 1 of Section 3.2.2.1, five plots were taken corresponding to the five samples. The source beam was applied at 300 mW and the samples cooled to 77K. The spectra are plotted together on one graph to show the wavelength span each encompasses relative to one another. Each is scaled along the intensity axis to be easily read; this does not represent the true relative scale each has to another. From the spectra (Figure 5.3), peak wavelength values are determined as shown in Table 5.1.

Table 5.1 Characteristics of samples under investigation.

Sample	Peak Wavelength (μm)	QW Type	QW Thickness (\AA) electrons(holes)	Waveguide Type	Active Region Effective Index
B	3.16	I	100	Tight	3.87
201-056	3.89	II	21.5(24)	Dilute	3.88
R1-73	3.76	II	21(24)	Dilute	3.88
R2-43	4.55	II	21(24)	Dilute	3.88
R0-62	4.125	II	21(24)	Tight	3.88

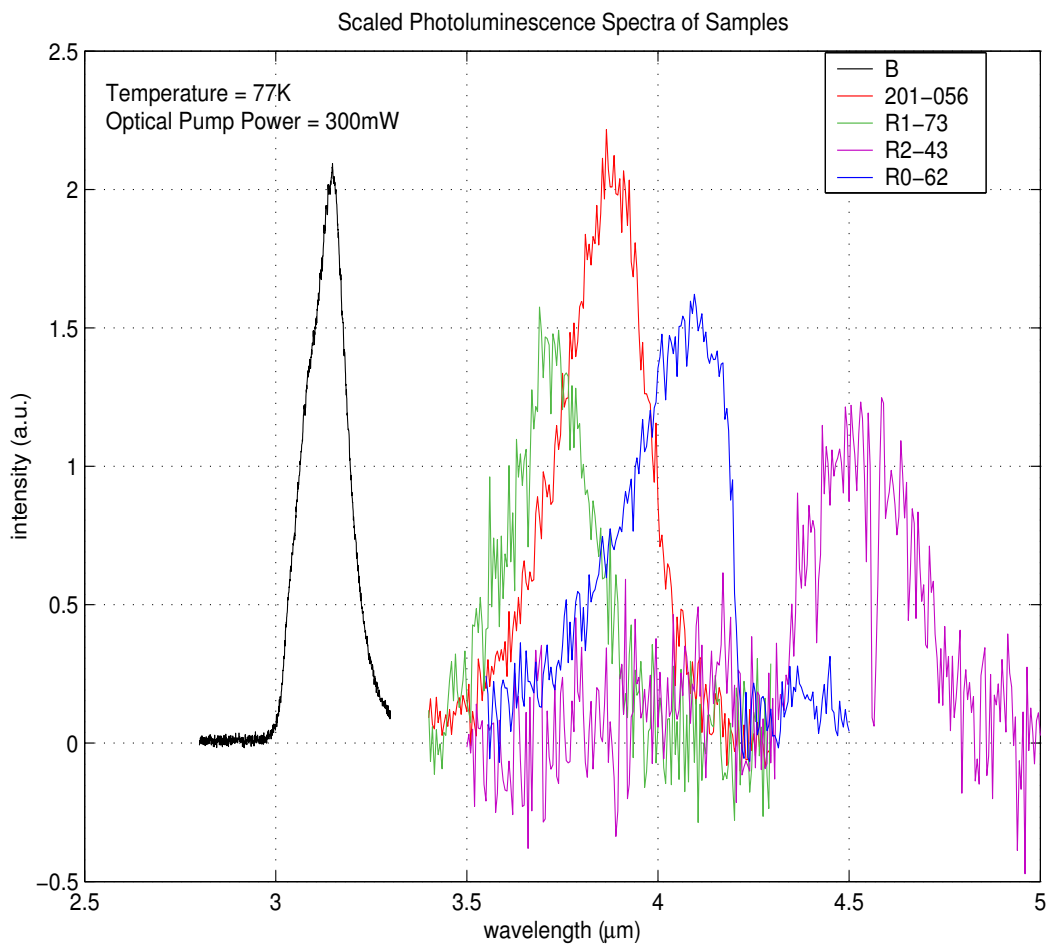


Figure 5.3 PL Spectra of the five different samples investigated. Relative intensities are not to scale.

5.3 Spontaneous Emission Results

Converting the experimental setup to the lasing configuration, the transformed Ti:Sapphire beam is applied to the samples as discussed in Chapter III. Using the peak wavelengths, the spectrometer is set to the proper resolution calculated from equation 4.3 for each sample. These settings are shown in Table 5.2.

Table 5.2 Spectrometer slit widths and grating increments used in data acquisition of emission spectra.

Sample	Slit Width (μm)	Grating Increment (nm)
R0-62	151	0.5
R2-43	184.5	1
R1-73	216	0.5 to 1 (varied)
201-056	195	0.2
B	193	0.1

The calculated slit-width settings are the largest that can be applied and still maintain the resolution needed to see Fabry-Perot resonances. The procedure for aligning the laser source beam onto a sample starts after the proper stripe has been formed and verified by the Beam Code system as described in Section 3.2.2.1. The mounted sample is positioned by translating the vacuum chamber along the x,y, and z axis until the stripe lies horizontally across the cleaved facets of the sample. The slits of the spectrometer are then opened fully, and the cylindrical lens rotated about its optical axis until a maximum signal is detected. The three-axis position of the sample is next fine tuned until the detected signal is maximized. These four actions are repeated as necessary until the maximum possible signal is detected. Afterward, the slits of the spectrometer are closed to the correct width and data is taken. If no lasing is seen, the adjustments are repeated until lasing occurs or further adjustments are exhausted.

Data taken for samples R0-62, R1-73, and R2-43 (shown in Figures 5.4 through 5.6) correlate with the model predictions presented in Section 5.1, *i.e.*, that lasing will not occur.

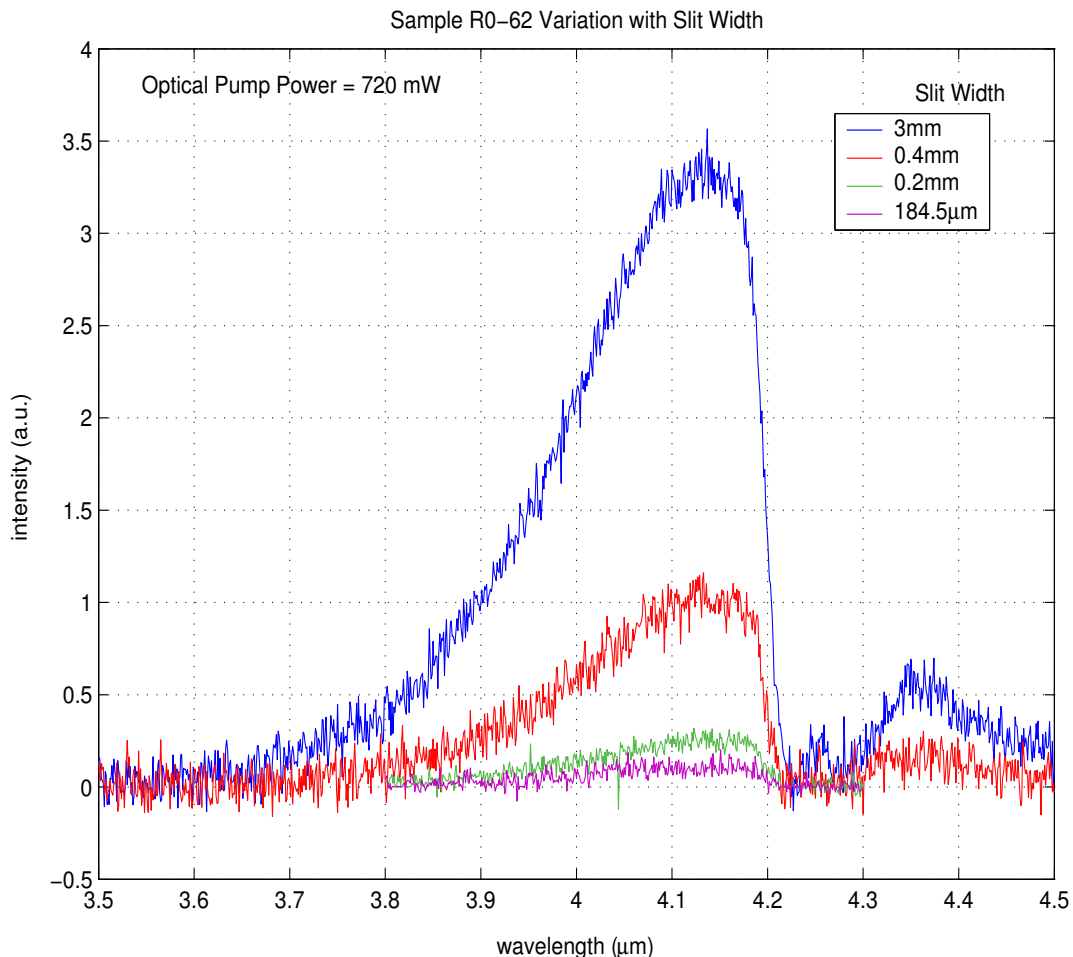


Figure 5.4 Spectra of Sample R0-62 taken as the spectrometer slit width is varied at a pump power of 720mW and temperature of 77K. No lasing or mode development is seen.

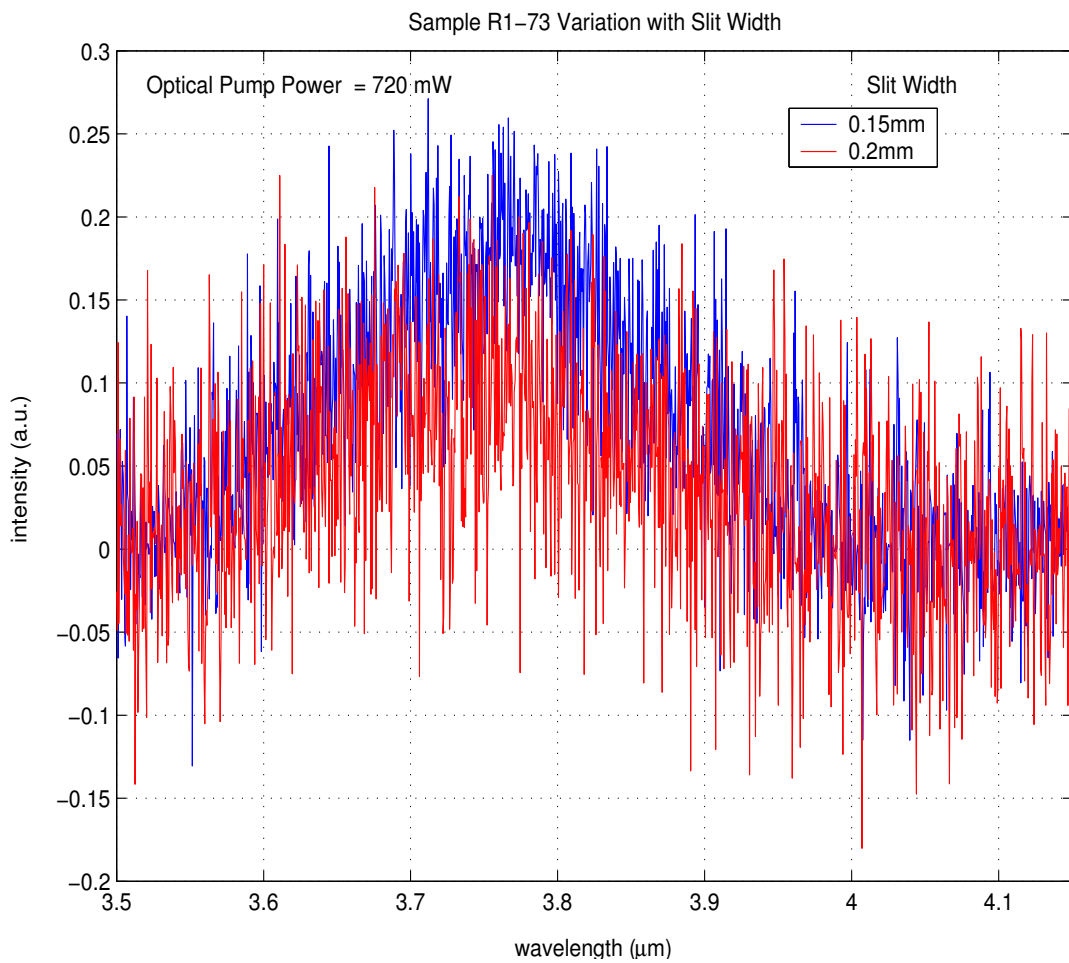


Figure 5.5 Spectra of Sample R1-73 taken as the spectrometer slit width is varied at a pump power of 720mW and temperature of 77K. No lasing or mode development is seen.

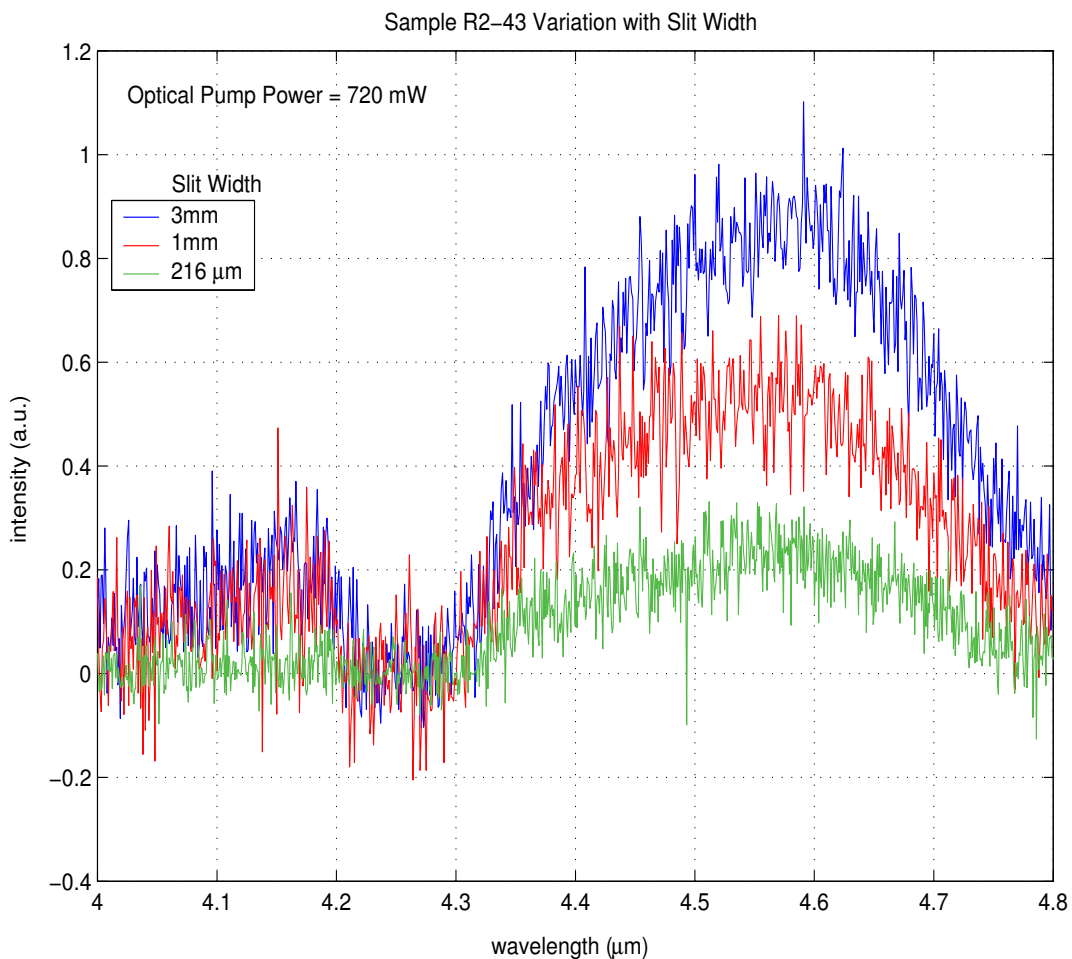


Figure 5.6 Spectra of Sample R2-43 taken as the spectrometer slit width is varied at a pump power of 720mW and temperature of 77K. No lasing or mode development is seen.

Evidence of stimulated emission cannot be seen in these plots as would be seen by Fabry-Perot oscillations along the crest of the PL curves. These oscillations are the longitudinal modes, discussed earlier, starting to form. The spectrometer slit width required to see oscillations, should they occur, cause these spectra to be very noisy because of the low intensity emitted by these samples. As the slit widths of the spectrometer decrease, less light is able to enter and soon only very high intensity light is able to pass into the spectrometer. From the light that does pass, only light at the appropriate wavelengths determined by the position of the grating are passed to the detector. Were stimulated emission to occur, the amount of light passed into the spectrometer would increase, raising the signal further above the background noise and, thus, causing the spectrum to be cleaner.

Because stimulated emission was not seen, the source beam power was increased in an attempt to reach lasing threshold. Cooling of the samples to liquid helium temperatures was also tried for this purpose. The spectra collected for samples R0-62, R1-73, and R2-43 varies little from that shown in Figures 5.4 through 5.6, indicating that only spontaneous emission is possible from these three samples using this experimental setup.

5.4 Stimulated Emission Results

Higher powers and lower temperatures did prove to work on samples 201-056 and B. The source beam power was increased to 2.37 watts, which is its maximum operating power. At this level, the signs of stimulated emission are seen in the Fabry-Perot mode development (oscillations) along the PL crest (see Figures 5.7 and 5.9). These oscillations are verified as being the formation of longitudinal modes when the samples are cooled to 7 K. The modes that occur at this temperature consistently overlap those at the higher temperature, showing the repeatability of the occurrence. This, in turn, confirms the detection of longitudinal modes and stimulated emission.

Plotting the spectrum versus frequency, the mode spacing is determined by taking the difference between mode peaks over the ridge of the spectrum and averaging. The mode spacing (longitudinal) is governed by equation 2.15 and is found to be 170.75 GHz for sample 201-056 and 169.37 GHz for sample B. This correlates well with the calculated spacing of 171 ± 1.7 GHz and 171 ± 1.1 GHz for the two samples, respectively. These values do not account for the uncertainty in the effective index of the active region, which were provided by the sample growers (see Table 5.1). Figures 5.7 to 5.9 show Fabry-Perot resonance for the two samples.

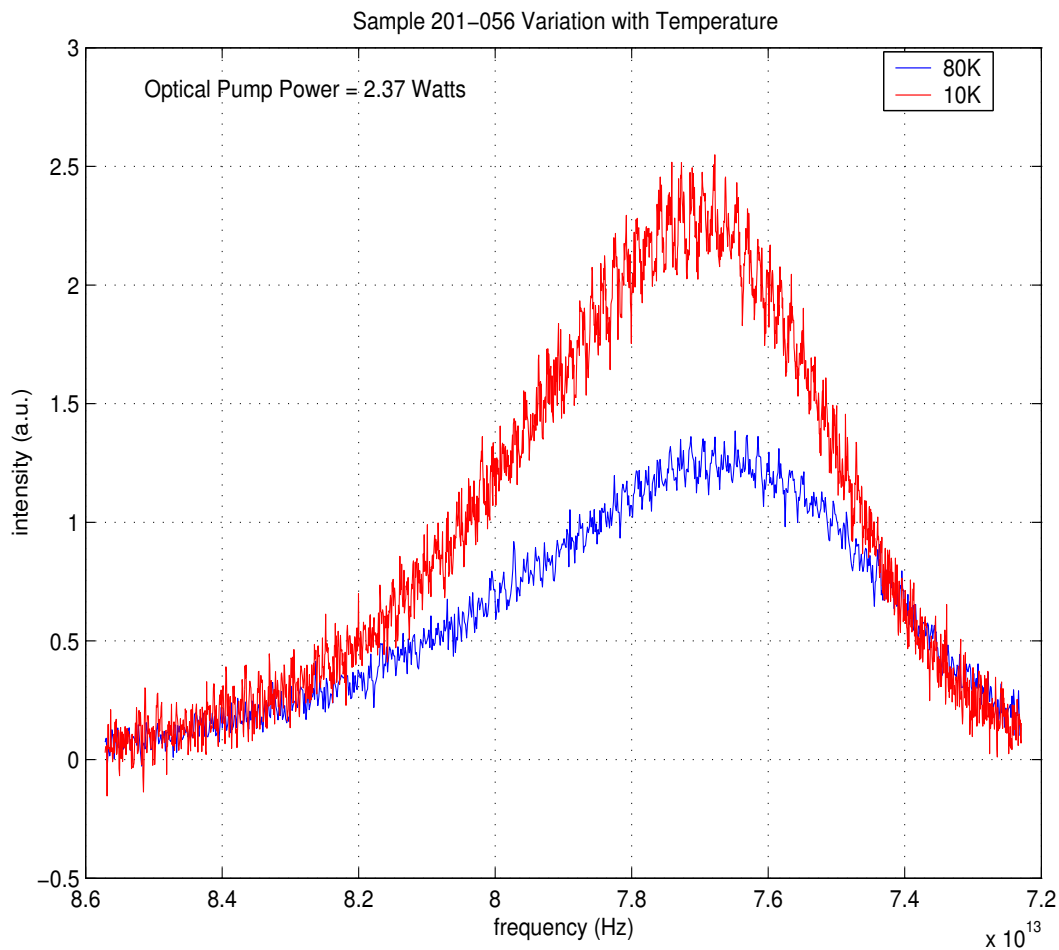


Figure 5.7 Spectra of Sample 201-056 taken at 80 and 10 K with 2.37 W excitation power. Longitudinal Mode development is seen along the crests of the two spectra.

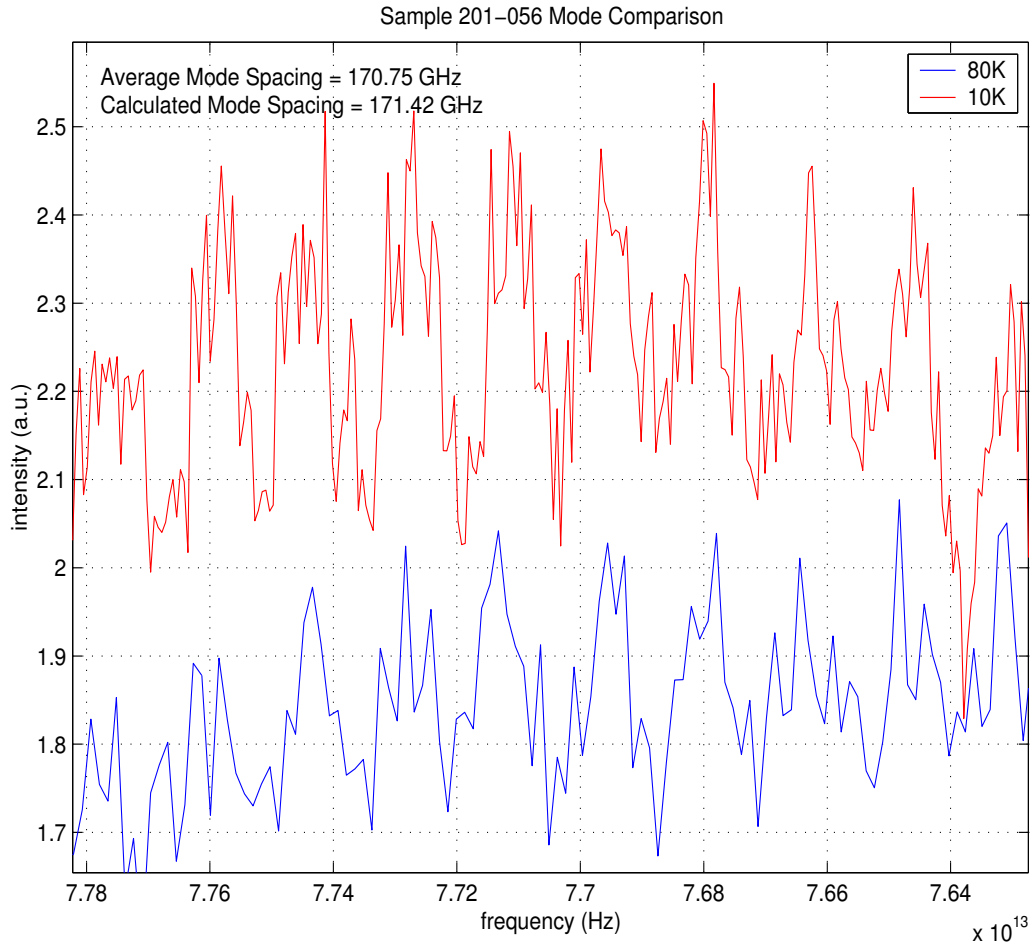


Figure 5.8 Close-up of spectra showing a high degree of mode overlap, confirming repeatability and thus mode formation. The longitudinal mode spacing is 170.75 ± 1.36 GHz.

As can be seen from Figure 5.7 for sample 201-056, lasing does not occur at the maximum pump power at low temperatures. This is attributed to retaining the 2300-Å GaSb cap layer having a bandgap energy of 0.726 eV. From equation 4.1, 60.1% of the Ti:Sapphire optical pump beam is absorbed in this layer due to being at a higher photon energy of 1.524 eV. Ideally, a pump having a photon energy less than 0.726 eV, or a wavelength higher than $1.709 \mu\text{m}$, is used to penetrate into the active region and stimulate emission. Comparing the spectra of samples R0-62, R1-73, and R2-43 (Figures 5.4–5.6) with sample 201-056, it is seen that retaining

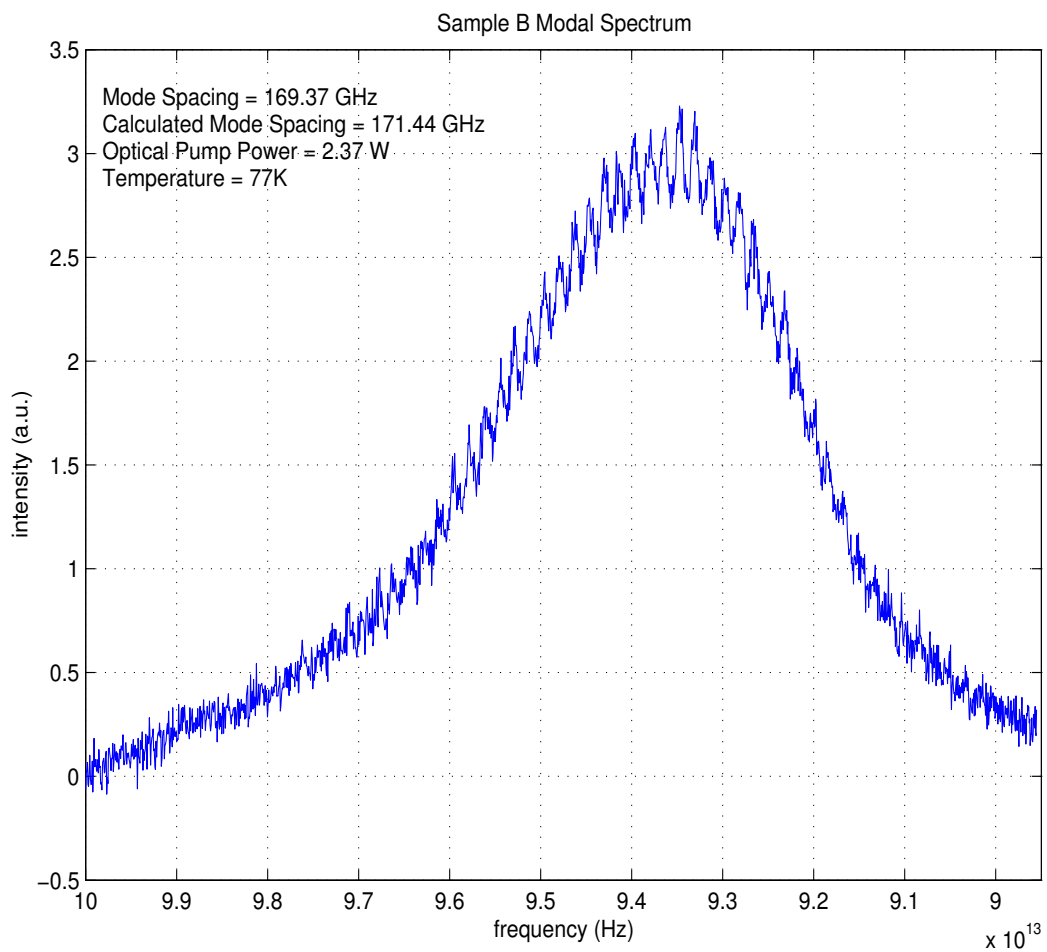


Figure 5.9 Spectrum of Sample B taken at 77 K with 2.37 W excitation power. Longitudinal mode development is seen along the crests of the spectrum. The mode spacing is 169.37 ± 0.58 GHz.

the cap layer of such structures is more beneficial than removing it because of the optical confinement it provides for stimulated emission. However, this layer must be transparent to the optical pump for enough energy to penetrate into the active region to produce lasing.

Even though lasing from sample 201-056 was not seen, the input power was varied for completeness to define where the modes cease to occur, indicating at what pump power stimulated emission transitions back to spontaneous emission. Figures 5.10 and 5.11 show this transition to take place near a pump power of 200 mW.

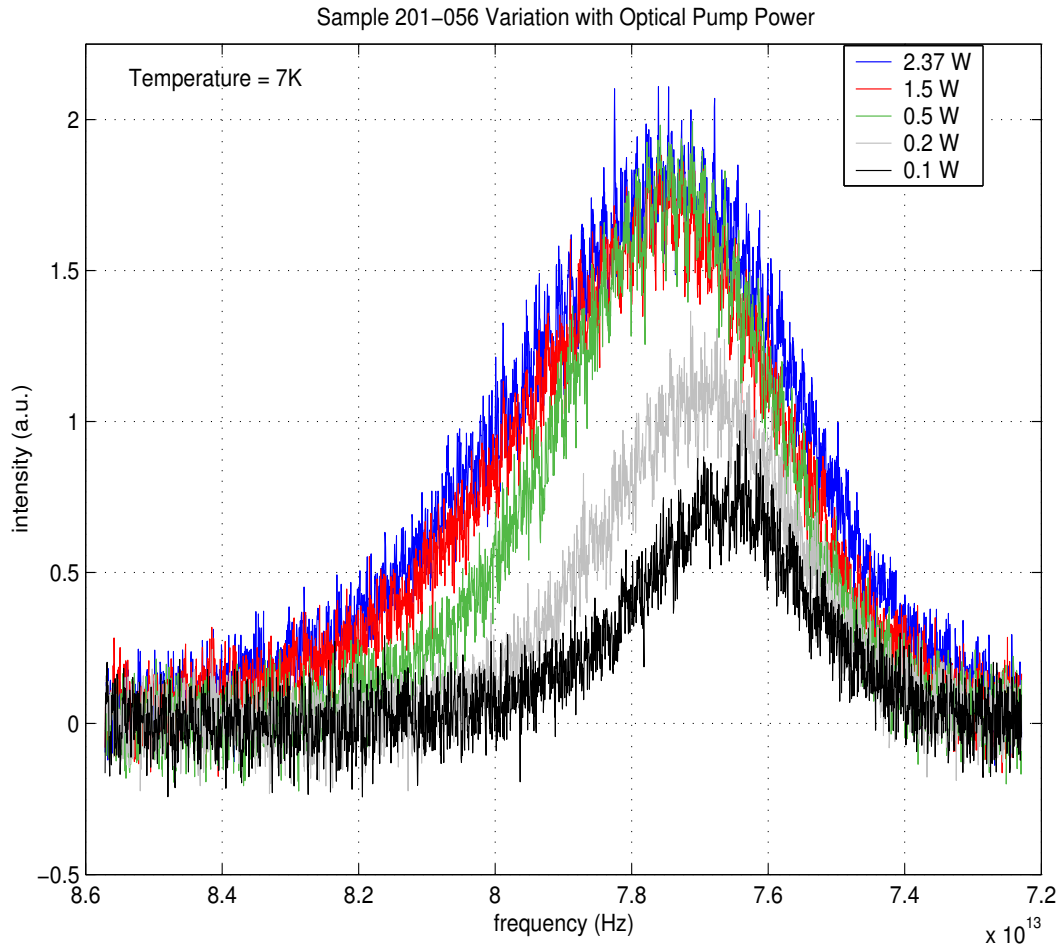


Figure 5.10 Spectra of Sample 201-056 taken as the source beam power is decreased from 2.37 W to 0.1 W.

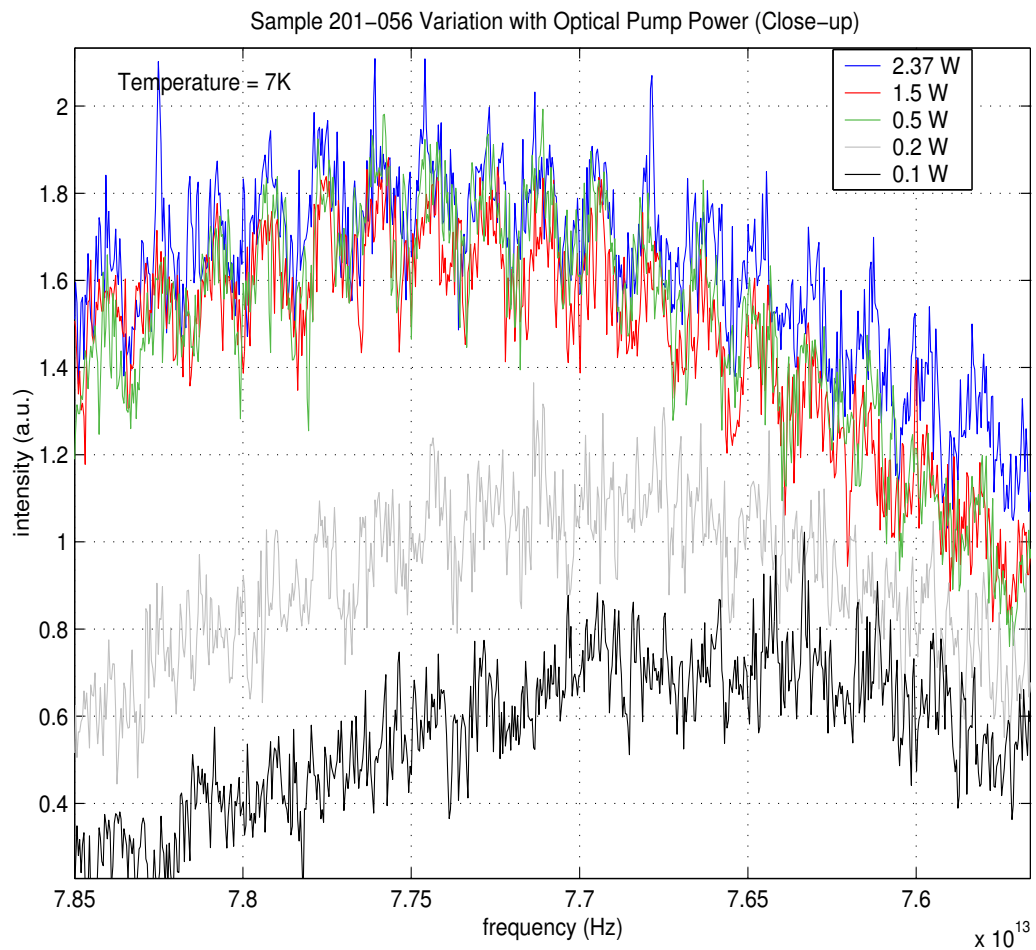


Figure 5.11 Close-up of Sample 201-056 spectra showing longitudinal modes ceasing to occur at 0.2 W.

5.5 Lasing Results

For sample B, it was found that laser emission did occur when the sample was cooled down to liquid helium temperatures. Figure 5.12 shows that the temperature drop allows population inversion to take place as is evident by the large peak in intensity that develops. The peak is actually made up of two lasing modes, which suggests that the gain could be increased further. From this point, the power was also varied to find where lasing ceases. An interesting occurrence was seen as this action was performed (Figure 5.13). At power levels between 2.37 W and 1.5 W, the lasing spectra changes little. At 1.5 W, the intensity peak of the lasing mode jumps to a higher level. From this power down, the peak steadily decreases until lasing ceases and only luminescence remains. This phenomenon is repeatable and is attributed to the heating that occurs when pumping at higher powers. A limit to the amount of energy that can be imparted to the system and transferred to the radiative emission process exists. Once this limit is passed, radiative transitions are saturated and non-radiative transitions increase. These non-radiative transitions impart energy into the semiconductor device in the form of heat. As the heat of the device builds, non-radiative recombination is increased even further.

5.6 Gain Calculation

The gain seen in Samples B and 201-056 is calculated using a technique developed by Hakki and Paoli [19] that incorporates the peak-to-valley ratio of each successive set of Fabry-Perot peaks in the intensity spectrum. The expression for the net gain is given by

$$\Gamma G_i = \frac{1}{L} \ln \left(\frac{r_i^{1/2} + 1}{r_i^{1/2} - 1} \right) + \frac{1}{L} \ln R \quad (5.1)$$

which is a function of wavelength. Here, L is the cavity length, R is the mirror reflectivity of a cleaved facet, r_i is the peak-to-valley ratio of the modes, and Γ is

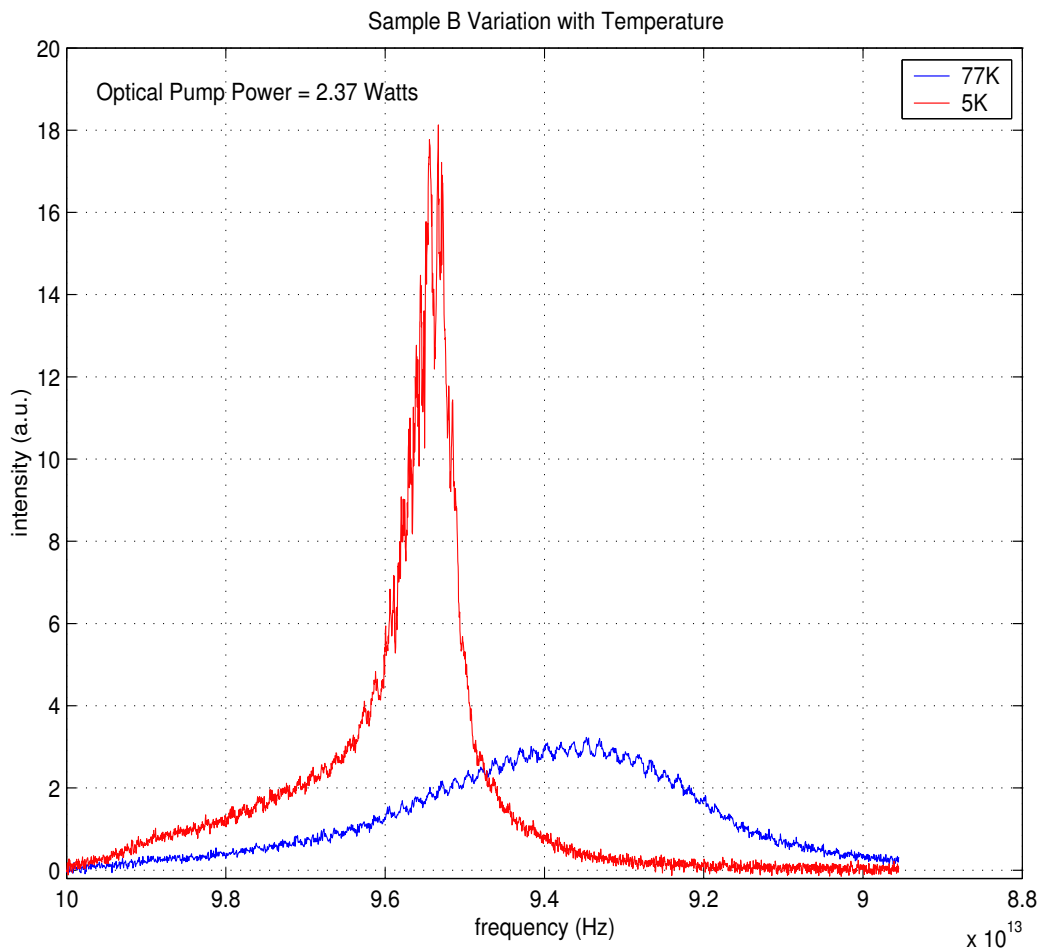


Figure 5.12 Spectra of Sample B taken at temperatures of 77K and 5K. Lasing is seen to occur at 5K as evident by the large intensity spike.

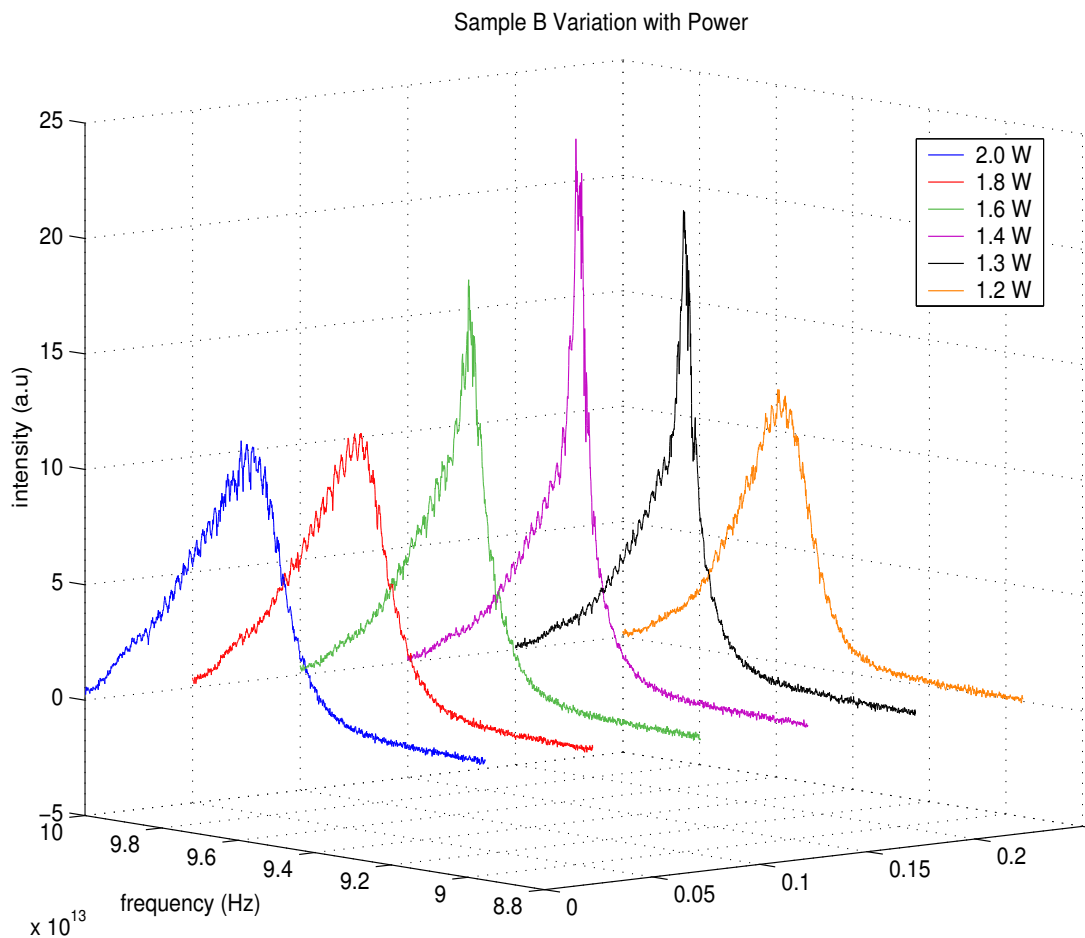


Figure 5.13 Spectra of Sample B taken at a temperature of 8K under varying pump powers. Saturation occurs at a pump power of 1.5 W and laser output is decreased at higher pump powers.

the electromagnetic filling factor. The mirror reflectivity was calculated using the equation $R = (1 - n_r)^2 / (1 + n_r)^2$ for the air/active region interface where n_r is the index of refraction of the active region as given in Table 5.1. The peak-to-valley ratio is computed by taking the average of the maximum values of two consecutive peaks, P_i and P_{i+1} , and dividing by the minimum value of the intermediate valley, V_i , to give the expression

$$r_i = \frac{P_i + P_{i+1}}{2V_i}. \quad (5.2)$$

This ratio represents the depth of modulation at each wavelength along the spectrum.

The filling factor is also a function of wavelength and is found by solving the electromagnetic boundary value problem for TE and TM modes in a waveguide. For the TE case, Γ is given by

$$\Gamma_{TE} = \left(1 + \frac{\sin(2\Psi)}{2\Psi}\right) \left[1 + \frac{1}{\Psi'} \left(\frac{A \cos \Psi^2}{\Psi}\right)^2\right]^{-1} \quad (5.3)$$

where $\Psi = k_x/2d$ and $\Psi' = (A^2 - \Psi^2)^{1/2}$ are found by solving the characteristic equation for the TE case, $\Psi \tan \Psi = \Psi'$, where k_x is the wavevector in the x-direction and d is the active region thickness. For the TM case, the characteristic equation becomes $(1 - \Delta n_r/n_r)^2 \Psi \tan \Psi = \Psi'$ where Δn_r is the difference in the refractive indices of the active region and the surrounding layers. For this case, the filling factor becomes

$$\Gamma_{TM} = \frac{\xi}{\xi + \zeta} \quad (5.4)$$

where

$$\xi = 1 + \left(1 + \frac{2\Psi^2}{\Psi_0^2}\right) \frac{\sin 2\Psi}{2\Psi},$$

$$\zeta = \left(1 - \frac{\Psi^2}{\Psi_0^2} + \frac{\Psi'^2}{\Psi_0^2}\right) \left(1 - \frac{\Delta n_r}{n_r}\right)^{-4} \frac{\cos^2 \Psi}{\Psi'},$$

$$\Psi_0 = \frac{2\pi n_r d}{\lambda}.$$

Incorporating this technique into Matlab® programs “Gainmodel2.m” and “Gainmodel2H.m” given in appendix B, the gain was computed for the TE and TM cases of both samples and is plotted versus wavelength in Figures 5.14 through 5.16. It is noted that the wavelength span shown in the plots does not span the full spectrum originally collected for these samples under the conditions shown. This is due to the Fabry-Perot modes being unresolvable out at the tails of the spectra. Thus, as many of the modes as can be resolved are included in the computation of the gain curves. The mirror reflectivities used were 0.348 and 0.347 for samples 201-056 and B, respectively. [19]

The jagged appearance of the curves is due to the low definition of the modes seen in the intensity spectra. Peaks and valleys are not well defined and cause the curves to fluctuate as shown. However, the overall shape of the curves is as expected for semiconductor laser gain curves. Loss is not seen and would be represented by negative gain values. Again, this is due to the noisy signal in the emission spectra, where Fabry-Perot resonance in the tails could not be resolved. If the tail sections could be included, it is expected that loss would be seen.

The occurrence of lasing confirms that the technique suggested in Section 3.2.2.1 was successful. This implies that laser structures can potentially be incorporated into the TRPL experiment. However, optically pumped lasing with the Ti:Sapphire pump source was only marginal with only one sample. A more appropriate source would be a fs-source operating at a $2\mu\text{m}$ wavelength.

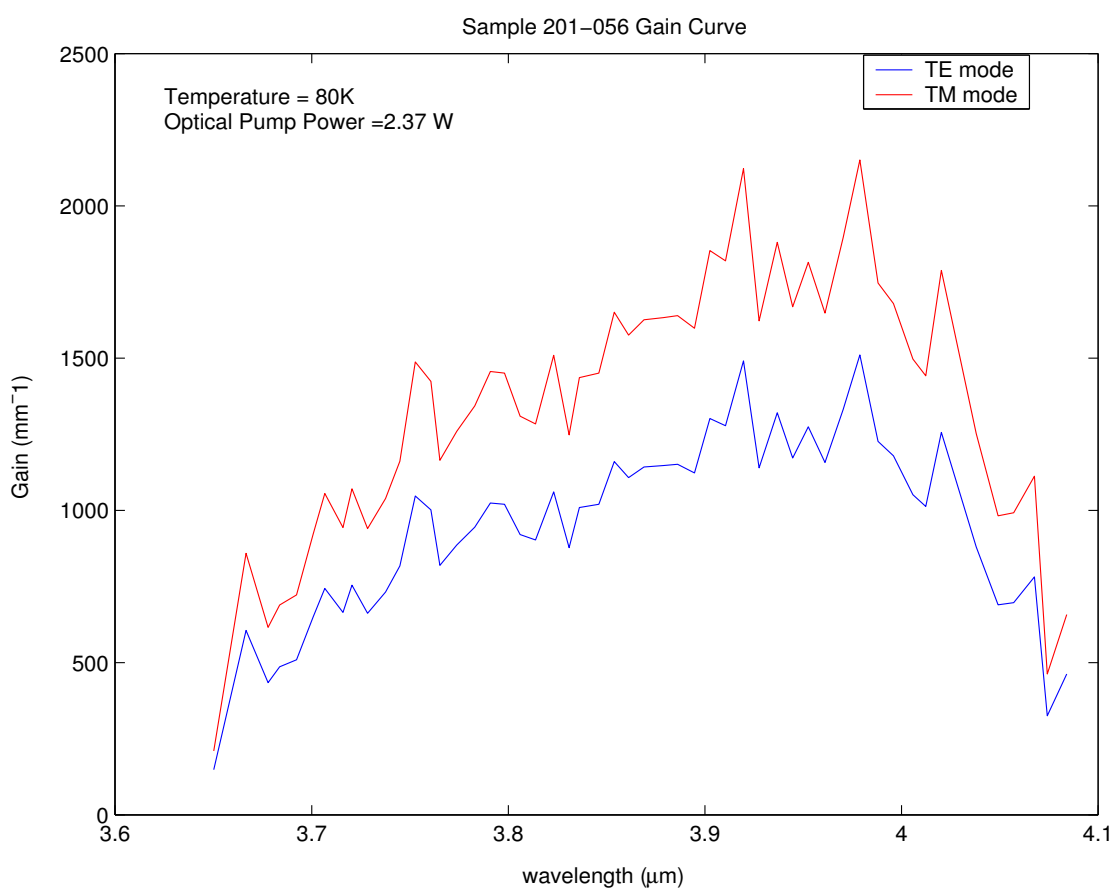


Figure 5.14 Gain curves of Sample 201-056 at 80K for the TE and TM modes.

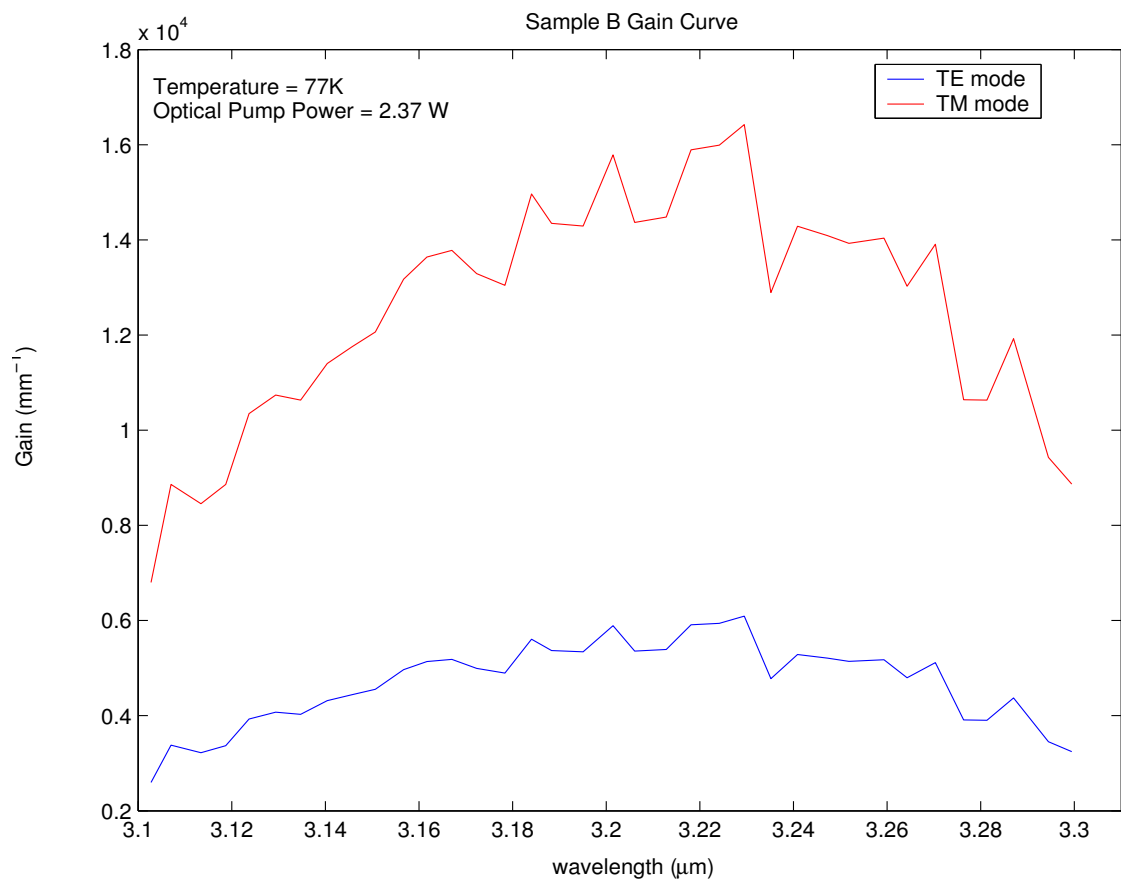


Figure 5.15 Gain curves of Sample B at 77K for the TE and TM modes.

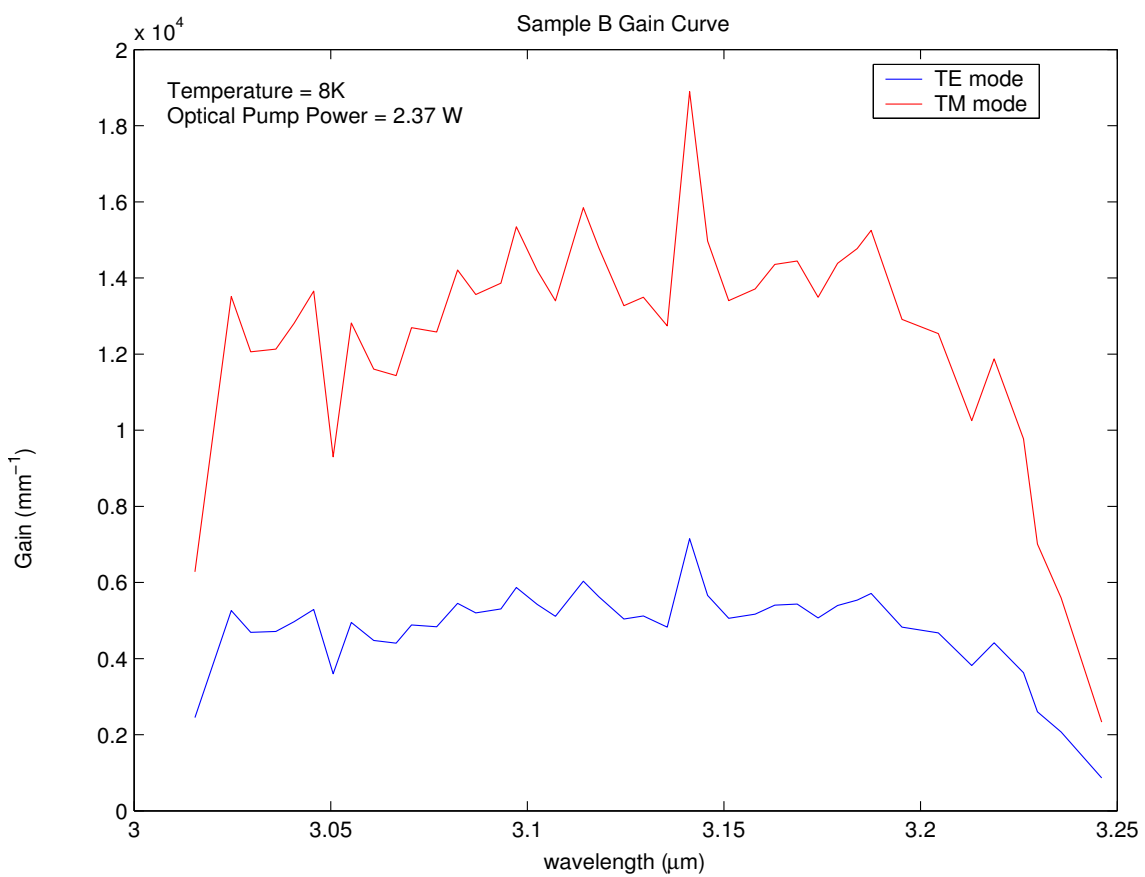


Figure 5.16 Gain curves of Sample B at 8K for the TE and TM modes.

5.7 Upconversion Results

To frequency up-convert laser emission in the TRPL experiment, it is first required to have TRPL in good working order. To accomplish this, Sample B is used because of its high luminescence signal as compared to the other samples. Sample B has also been investigated using the experiment previously, and has supplied a baseline needed to distinguish whether or not the experiment is properly set up and running. The optical alignment is carried out as described in Chapter III. The critical aspects of this experiment lie in positioning the non-linear crystal to the correct rotation angle, as called for by the governing equations, while overlapping the pump and signal beam to within $\pm 12.5 \mu\text{m}$ within the crystal for wave mixing. The angle is calculated to be 16.3° . Since the luminescence of the sample contains multiple wavelengths, angles to either side of this can be used. Therefore, the planar acceptance angle must be calculated to determine the range of angles where upconversion is expected to be seen. First, the solid angle that upconversion can take place over is calculated. This angle is centered around the phase-matching angle and is given by

$$\Delta\phi = \frac{2.78n\lambda_{pl}}{L \left(1 - \frac{n\lambda_{SFG}}{\theta n\lambda_{pl}} \right)} \quad (5.5)$$

where L is the crystal thickness [33]. The indices of refraction seen by the two entering beams depend on their respective wavelengths. For the PL beam, $n = 1.75$ and for the upconverted beam, $n = 1.81$. The calculated acceptance solid angle is thus $\Delta\phi = 0.021$ steradians which is converted to a planar angle of

$$\theta_{\max} = \cos^{-1} \left(1 - \frac{\phi}{2\pi} \right) = 4.686^\circ. \quad (5.6)$$

Under these conditions, upconversion of the PL signal from sample B was found to occur at $16.5 \pm 1^\circ$ which is within the calculated rotation window of $16.3 \pm 4.7^\circ$.

The upconverted signal is seen in Figure 5.17. At time delays less than 0 ps, no signal is detected as is expected. At 0 ps, where both path lengths of the TRPL experiment are equal, the signal jumps up in intensity. From this zero time delay point on, the signal is seen to quickly reach its peak value and then slowly die off as is expected. This confirms the production and detection of the upconverted PL signal and shows the time decay of that signal. Attempts were made to refine this signal, but due to time constraints, further optimization was not achieved.

With this success and the successful development of a technique to produce laser emission from Sample B, the building blocks to study QW laser structures using the TRPL experiment are now in place.

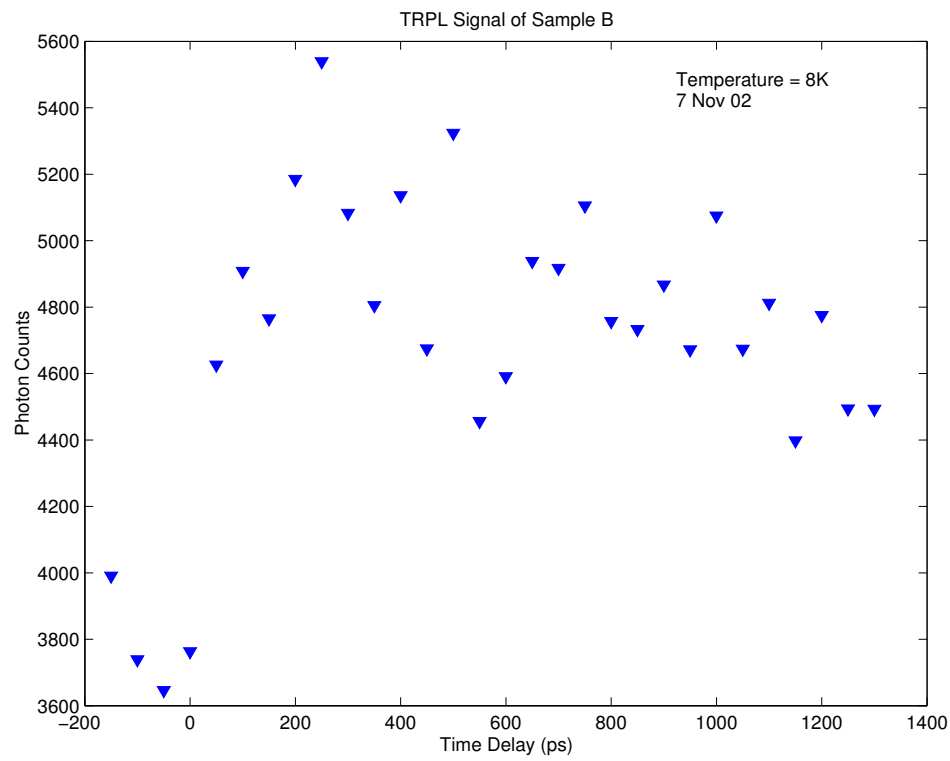


Figure 5.17 TRPL signal of sample B on 7 Nov 02.

VI. Conclusion

The objective of this research was to study the modal development of mid-IR laser structures using ultra-fast spectroscopy to see how “ghost” modes effect the overall output. The goal was to incorporate a laser structure into a time-resolved photoluminescence experiment in order to do so. This chapter summarizes this effort and presents suggestions for future work.

6.1 Summary

Five laser structures were studied with the intent of producing laser emission from each. The transverse mode development was first predicted using a model for the dilute wave-guide structures with the cap layer etched away. Although etching the cap layer was necessary for penetration of the pump laser into the active region, only “ghost” modes were predicted by the model under this configuration, and detectable laser emission was not expected. The TRPL experiment was modified by first taking PL spectrums of the samples to obtain an estimate of the lasing wavelength. Next, the optical path of the pump beam was modified to stimulate lasing from the samples. The samples were also prepared, to aid in this process, by cleaving the structures along two parallel crystal planes forming Fabry-Perot resonant cavities. Data taken from the etched samples show no laser emission, as predicted by the model. The removal of the cap layer significantly reduces the device’s ability to confine optical radiation and thus to lase.

Laser emission was seen from the two types of structures that remained unetched. For the type-II laser, stimulated emission was seen below threshold in the form of Fabry-Perot resonance, but lasing was not achieved. This sample retained a 2300-Å cap layer of GaSb, absorbing enough of the optical pump to keep it from attaining population inversion and, thus, lasing. For the type-I laser, population inversion was created producing laser emission. Data taken for this device showed the

effects of non-radiative processes as the optical pump power levels were varied. High powers produced sub-lasing emission, while lower powers produced a well defined emission peak. This indicates that non-radiative transitions become dominant at higher powers causing device heating and lower emission. Using the emission spectra of the two un-etched samples, the gain was computed for the TE and TM cases. Both samples show gain curves consistent in overall trend with expected results. The complete gain curve could not be determined since the tails of the emission spectrum cannot be included due to poor resolution.

TRPL was attempted as the final step in the process, using the frequency upconverted signal of sample B as a baseline to verify that correct alignment of the experiment. Upconversion was achieved at a nonlinear crystal tilt angle of $16.5 \pm 1^\circ$. The success of laser production and PL upconversion from this sample lays the necessary groundwork for the investigation of modal development in semiconductor QW laser devices using TRPL.

6.2 Future Work

To further work on this project, two areas of the experiment need attention. Foremost, the experiment must be fine tuned to achieve a well-defined upconversion signal. This can be done by paying careful attention to the optical alignment to achieve the proper overlap inside the nonlinear crystal. Secondly, a source laser operating in the $2\text{-}\mu\text{m}$ wavelength range is needed to prevent absorption in the GaSb cap layers of the devices. This will enable the proper stimulation of the active region while retaining the optical confinement needed to produce lasing. This source must also retain sub-pico-second pulses for the experiment to work properly. To accomplish this, an optical parametric oscillator (OPO) could be used to convert the wavelength of the Ti:Sapphire laser. Alternatively, the GaSb cap layers of the samples could be replaced with an oxide, such as TiO_2 , to prevent absorption.

The success of laser production shows that the TRPL experiment can be modified to produce such emission. It is expected that upconversion of this laser emission will produce much stronger TRPL signals. Therefore, to increase laser emission, the optical pumping technique should be modified to include a larger focal-length cylindrical lens. The current lens requires placement very near the vacuum chamber, limiting its movement and preventing the focused strip from being fine tuned. Incorporating a larger focal-length lens will allow more movement allowing the laser stripe to be better focused.

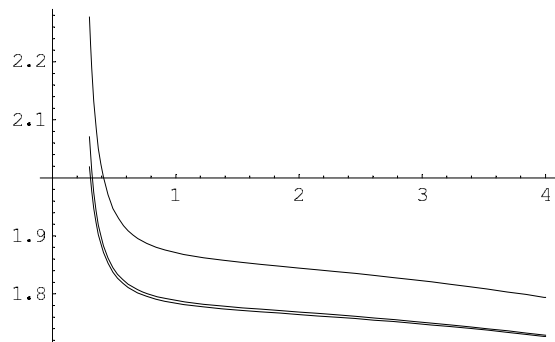
With these modifications, the TRPL experiment can be expanded to better investigate laser devices. This includes further study of the lasing roll-over that occurs as a function of pump power. This phenomenon may prove to be linked with the TEM mode development in laser devices, giving insight into “ghost” modes and their nature. Once configured for lasing, the TRPL experiment will be a valuable tool for mode investigation.

Appendix A. Calculation of Non-Linear Crystal Tilt Angle

```
(*oeo sum-frequency generation (upconversion) w/ KTA*)

(*Index ellipsoid for KTA*)
nx[λ_] := Sqrt[1.90713 + 1.23522 / (1 - (0.19692 / λ)^2) - 0.01025 λ^2]
(*nx (λ) for KTA, λ in μm*)
ny[λ_] := Sqrt[2.15912 + 1.00099 / (1 - (0.21844 / λ)^2) - 0.01096 λ^2]
(*ny (λ) for KTA, λ in μm*)
nz[λ_] := Sqrt[2.14786 + 1.29559 / (1 - (0.22719 / λ)^2) - 0.01436 λ^2]
(*nz (λ) for KTA, λ in μm*)

Plot[{nx[λ], ny[λ], nz[λ]}, {λ, 0.3, 4}]
```



- Graphics -

```
λPL = 3.16 (*peak wavelength for InAs sample, in μm*)
λPump = 0.808 (*Ti:Sapphire laser wavelength in μm*)
λSFG = 1 / (1 / λPL + 1 / λPump) (*Up-converted wavelength in μm*)
```

3.16

0.808

0.643468

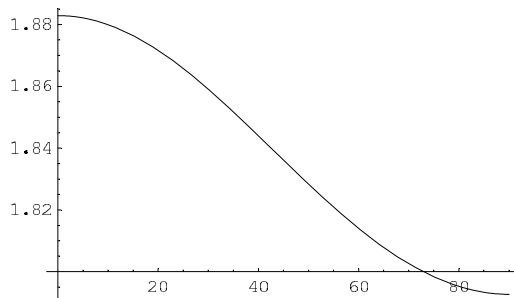
```

ny[λPL]
nx[λPump]
nz[λPump]
ny[λSFG]
1.74799
1.79267
1.8829
1.81272

(*Extraordinary index for Pump wavelength for angle,
θCrysPump, in crystal relative to x-axis*)
nePump[θCrysPump_] := nx[λPump]
nz[λPump] / √(nx[λPump] Cos[Pi θCrysPump / 180])^2 + (nz[λPump] Sin[Pi θCrysPump / 180])^2

Plot[nePump[θCrysPump], {θCrysPump, 0, 90}]

```

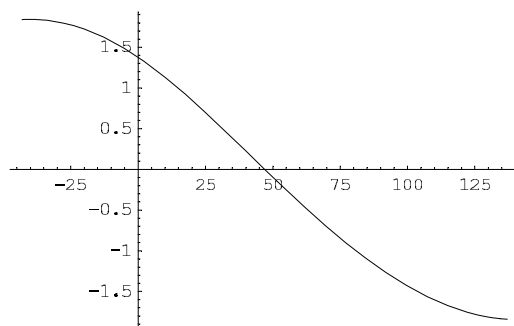


- Graphics -

```

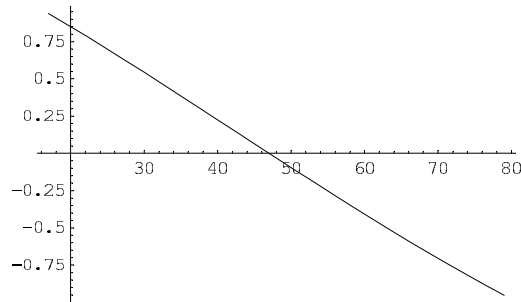
(*Snell's Law: Solve for θCrysPL (θCrysPump) inside the crystal,
relative to x-axis*)
Plot[nePump[θCrysPump] Sin[(47 - θCrysPump) Pi / 180], {θCrysPump, -43, 137}]
(*Note: 43° crystal cut*)

```



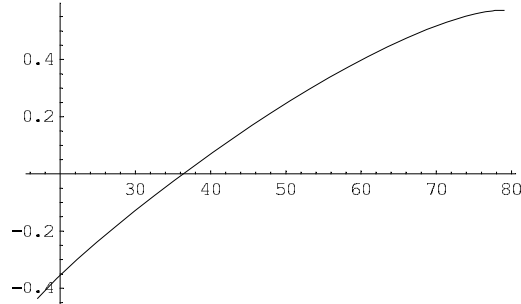
- Graphics -

```
Plot[nePump[θCrysPump] Sin[(47 - θCrysPump) Pi / 180], {θCrysPump, 17, 79}]
```



▪ Graphics ▪

```
Plot[Sin[Pi (20 - 180 ArcSin[nePump[θCrysPump] Sin[(47 - θCrysPump) Pi / 180]] / Pi) / 180] / ny[λPL], {θCrysPump, 17, 79}]  
(*Note: 20° between θPump and θPL outside the crystal*)
```

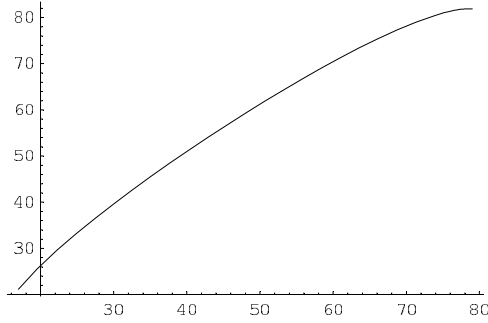


▪ Graphics ▪

```

Plot[180 ArcSin[
  Sin[Pi (20 - 180 ArcSin[nePump[θCrysPump] Sin[(47 - θCrysPump) Pi / 180]] / Pi) / 180]
  /ny[λPL]] /Pi + 47, {θCrysPump, 17, 79}]
(*This is θCrysPL (θCrysPump) inside the crystal, relative to the x-axis*)

```



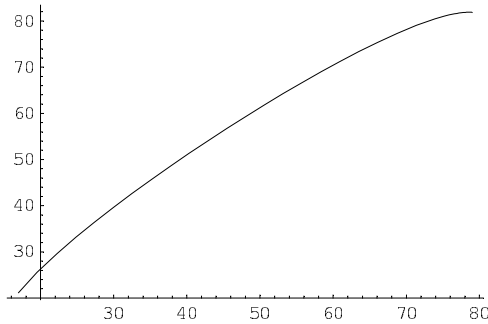
▪ Graphics ▪

```

θCrysPL[θCrysPump_] := 180 ArcSin[
  Sin[Pi (20 - 180 ArcSin[nePump[θCrysPump] Sin[(47 - θCrysPump) Pi / 180]] / Pi) / 180]
  /ny[λPL]] /Pi + 47

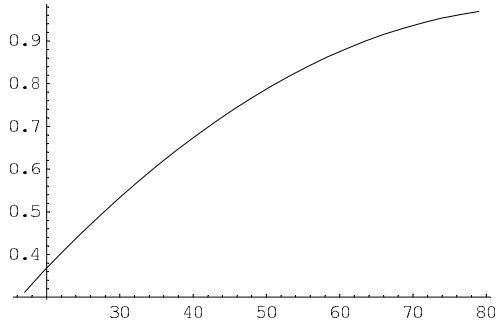
```

```
Plot[θCrysPL[θCrysPump], {θCrysPump, 17, 79}]
```



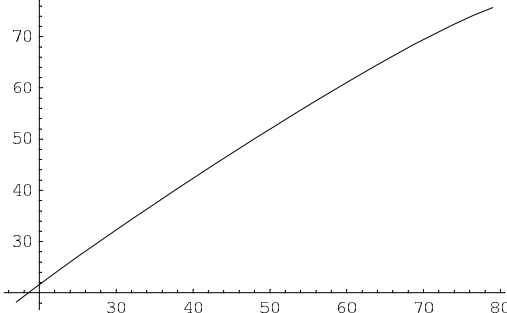
▪ Graphics ▪

```
(*Use phase-matching equations to find unique θCrysSFG*)
Plot[(ny[λPL] Sin[Pi θCrysPL[θCrysPump] / 180] / λPL +
nePump[θCrysPump] Sin[Pi θCrysPump / 180] / λPump) λSFG / ny[λSFG], {θCrysPump, 17, 79}]
```



- Graphics -

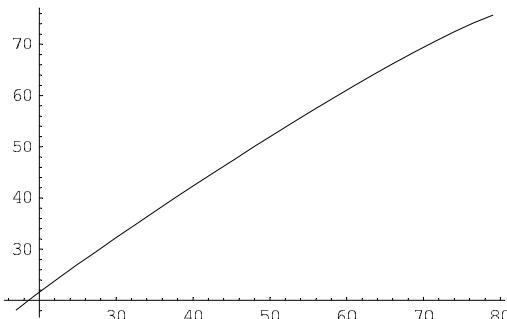
```
Plot[180 ArcSin[(ny[λPL] Sin[Pi θCrysPL[θCrysPump] / 180] / λPL + nePump[θCrysPump]
Sin[Pi θCrysPump / 180] / λPump) λSFG / ny[λSFG]] / Pi, {θCrysPump, 17, 79}]
```



- Graphics -

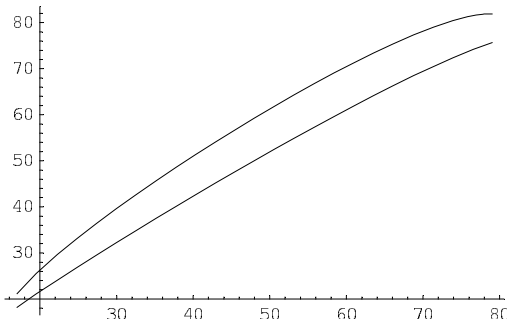
```
θCrysSFG1[θCrysPump_] :=
180 ArcSin[(ny[λPL] Sin[Pi θCrysPL[θCrysPump] / 180] / λPL + nePump[θCrysPump]
Sin[Pi θCrysPump / 180] / λPump) λSFG / ny[λSFG]] / Pi
```

```
Plot[\thetaCrysSFG1[\thetaCrysPump], {\thetaCrysPump, 17, 79}]
```



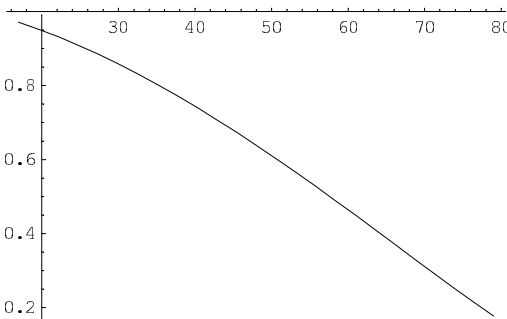
- Graphics -

```
Plot[{θCrysPL[θCrysPump], θCrysSFG1[θCrysPump]}, {θCrysPump, 17, 79}]
```



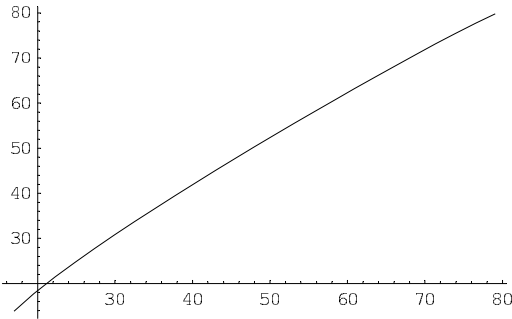
- Graphics -

```
Plot[(ny[λPL] Cos[Pi θCrysPL[θCrysPump]/180]/λPL +  
nePump[θCrysPump] Cos[Pi θCrysPump/180]/λPump) λSFG/ny[λSFG], {θCrysPump, 17, 79}]
```



- Graphics -

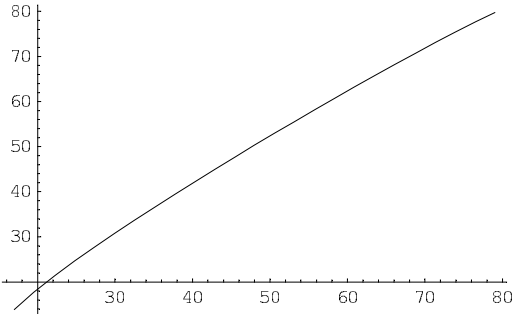
```
Plot[180 ArcCos[(ny[\lambdaPL] Cos[Pi \thetaCrysPL[\thetaCrysPump] / 180] / \lambdaPL + nePump[\thetaCrysPump]
Cos[Pi \thetaCrysPump / 180] / \lambdaPump) \lambdaSFG / ny[\lambdaSFG]] / Pi, {\thetaCrysPump, 17, 79}]
```



▪ Graphics ▪

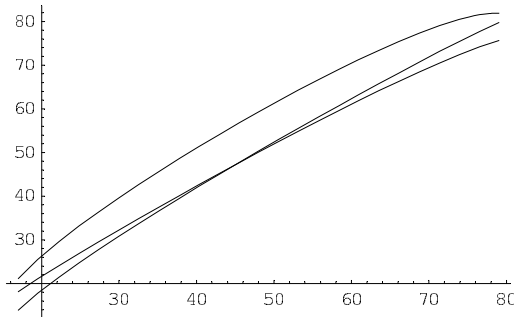
```
\thetaCrysSFG2[\thetaCrysPump_] :=  
180 ArcCos[(ny[\lambdaPL] Cos[Pi \thetaCrysPL[\thetaCrysPump] / 180] / \lambdaPL + nePump[\thetaCrysPump]
Cos[Pi \thetaCrysPump / 180] / \lambdaPump) \lambdaSFG / ny[\lambdaSFG]] / Pi
```

```
Plot[\thetaCrysSFG2[\thetaCrysPump], {\thetaCrysPump, 17, 79}]
```



▪ Graphics ▪

```
Plot[{θCrysPL[θCrysPump], θCrysSFG1[θCrysPump], θCrysSFG2[θCrysPump]}, {θCrysPump, 17, 79}]
```



- Graphics -

```
FindRoot[θCrysSFG1[θCrysPump] == θCrysSFG2[θCrysPump], {θCrysPump, 42}]

{θCrysPump → 44.9551}
```

```
θCrysPL[45.00116399070333`]
θCrysSFG1[45.00116399070333`]
```

56.2554

47.1954

```
(*Crystal rotation = θPL outside the crystal, relative to crystal normal*)
θRot[θCrysPump_] := 180 ArcSin[ny[λPL] Sin[Pi (θCrysPL[θCrysPump] - 47) / 180]] / Pi
```

```
θRot[45.00116399070333`]
```

16.3281

```
(*θSFG outside crystal, relative to crystal normal is...*)
θSFGOut[θCrysPump_] := 180 ArcSin[ny[λSFG] Sin[Pi (θCrysSFG1[θCrysPump] - 47) / 180]] / Pi
```

```
θSFGOut[45.00116399070333`]
```

0.354271

Appendix B. Gain Calculation Programs for TE and TM Modes

```

function[Gain,gamma]=gainmodel2(lambda,p,v,L,nr,nc,d)
% This function calculates the gain of the **TE** mode given the inputs
% above using the technique developed by Hakki and Paoli.
%
% lambda = i vector containing the wavelengths corresponding to the valleys v
% p     = i+1 vector containing the peak values
% v     = i vector containing the valley values
% L     = Cavity length of laser device
% nr    = effective index in the active region
% nc    = effective index in the layer surrounding the active region
% d     = active region thickness
%
% By Lt Gabe Mounce for AFIT Thesis
% Date: Jan 30, 2003
% Ref: Hakki, B.W. and T. L. Paoli, "Gain Spectra in GaAs Double-
%       -Heterostructure Injection Lasers," Journal of Applied Physics, 46(3):1299-1306
%       (March 1975)

% lambda1=lambda.*(10^-6);
last=length(lambda);
for index=1:last
    gamma(index,1)=ff(lambda(index),nr,nc,d); %function to solve for gamma
end
clear index

%Calculation of peak-to-valley ratio used in gain equation
for index=1:length(p)-1
    r(index,1)=(p(index)+p(index+1))/(2*v(index));
end

% Gain equation-----
% Gain=(1./L.*gamma).*log((sqrt(r)+1)./(sqrt(r)-1))+(log(0.99)./(L.*gamma));
front=(1./L.*gamma).*log((sqrt(r)+1)./(sqrt(r)-1));
back=(log(0.347)./(L.*gamma));
Gain=front+back;

```

```

function[gamma]=ff(lambda,nr,nc,d);
% This function calculates the filling factor, gamma, for the **TE** mode given the
inputs
% above. This is done by solving the characteristic equation for the TE case.
%
% lambda = i vector containing the wavelengths corresponding to the valleys v
% nr    = effective index in the active region
% nc    = effective index in the layer surrounding the active region
% d     = active region thickness
%
% By Lt Gabe Mounce for AFIT Thesis
% Date: Jan 30, 2003
% Ref: Hakki, B.W. and T. L. Paoli, "Gain Spectra in GaAs Double-
%       -Heterostructure Injection Lasers," Journal of Applied Physics, 46(3):1299-1306
%       (March 1975)

% nr=3.88;
% nc=3.82;
deltan=nr-nc; % difference in effective index between the active and surrounding layers
% d=21.273e-6; %Active Region Thickness in microns
% lambda=3.80499195728567e-006;
lambda=lambda*(10^-6); % Wavelength in microns
A=(pi*nr^2*d/lambda)^2*((2*deltan*nr-deltan^2)/nr^2);
kx=146500; %for sample 201-056
% kx=2667900; % For sample B

RHS=sqrt(A^2-(kx.*d/2).^2); %Right Hand side of characteristic equation

LHS=(kx.*d/2).*tan(kx.*d/2); % Left hand side of characteristic equation

% Step process to converge on the solution when RHS=LHS.
while abs(RHS-LHS) > 0.1
    if LHS > RHS
        kx=kx-10;
    elseif LHS < RHS
        kx=kx+10;
    end
    RHS=sqrt(A^2-(kx.*d/2).^2);
    LHS=(kx.*d/2).*tan(kx.*d/2);
end

```

```

end
RHS=sqrt(A^2-(kx.*d/2).^2);
LHS=(kx.*d/2).*tan(kx.*d/2);
end

while abs(RHS-LHS) > 0.001
if LHS > RHS
    kx=kx-0.1;
elseif LHS < RHS
    kx=kx+0.1;
end
RHS=sqrt(A^2-(kx.*d/2).^2);
LHS=(kx.*d/2).*tan(kx.*d/2);
end

while abs(RHS-LHS) > 0.0001
if LHS > RHS
    kx=kx-0.01;
elseif LHS < RHS
    kx=kx+0.01;
end
RHS=sqrt(A^2-(kx.*d/2).^2);
LHS=(kx.*d/2).*tan(kx.*d/2);
end

while abs(RHS-LHS) > 0.00001
if LHS > RHS
    kx=kx-0.001;
elseif LHS < RHS
    kx=kx+0.001;
end
RHS=sqrt(A^2-(kx.*d/2).^2);
LHS=(kx.*d/2).*tan(kx.*d/2);
end

while abs(RHS-LHS) > 0.000001
if LHS > RHS
    kx=kx-0.0001;
elseif LHS < RHS
    kx=kx+0.0001;
end

```

```
psi=kx*d/2;  
top=(1+sin(2*psi)/(2*psi));  
bottom=1+(1/RHS)*(A*(cos(psi))^2/psi)^2;  
gamma=top/bottom;
```

```

function[Gain, gamma]=gainmodel2H(lambda,p,v,L,nr,nc,d)
% This function calculates the gain of the **TM** mode given the inputs
% above using the technique developed by Hakki and Paoli.
%
% lambda = i vector containing the wavelengths corresponding to the valleys v
% p     = i+1 vector containing the peak values
% v     = i vector containing the valley values
% L     = Cavity length of laser device
% nr    = effective index in the active region
% nc    = effective index in the layer surrounding the active region
% d     = active region thickness
%
% By Lt Gabe Mounce for AFIT Thesis
% Date: Jan 30, 2003
% Ref: Hakki, B.W. and T. L. Paoli, "Gain Spectra in GaAs Double-
%       -Heterostructure Injection Lasers," Journal of Applied Physics, 46(3):1299-1306
%       (March 1975)

% lambda1=lambda.*(10^-6);
last=length(lambda);
for index=1:last
    gamma(index,1)=FFH(lambda(index),nr,nc,d); % Function to solve for gamma
end

clear index

%Calculation of peak-to-valley ratio used in gain equation
for index=1:length(p)-1
    r(index,1)=(p(index)+p(index+1))/(2*v(index));
end

% Gain equation-----
% Gain=(1./L.*gamma).*log((sqrt(r)+1)./(sqrt(r)-1))+(log(0.99)./(L.*gamma));
front=(1./L.*gamma).*log((sqrt(r)+1)./(sqrt(r)-1));
back=(log(0.347)./(L.*gamma));

Gain=front+back;

```

```

function[gamma]=ffh(lambda,nr,nc,d);
% This function calculates the filling factor, gamma, for the **TM** mode given the
inputs
% above. This is done by solving the characteristic equation for the TM case.
%
% lambda = i vector containing the wavelengths corresponding to the valleys v
% nr    = effective index in the active region
% nc    = effective index in the layer surrounding the active region
% d     = active region thickness
%
% By Lt Gabe Mounce for AFIT Thesis
% Date: Jan 30, 2003
% Ref: Hakki, B.W. and T. L. Paoli, "Gain Spectra in GaAs Double-
%       -Heterostructure Injection Lasers," Journal of Applied Physics, 46(3):1299-1306
%       (March 1975)

% nr=3.88;
% nc=3.82;
deltan=nr-nc; % difference in effective index between the active and surrounding layers
% d=21.273e-6; %Active Region Thickness in microns
% lambda=3.80499195728567e-006;
lambda1=lambda*(10^-6); % Wavelength in microns
A=(pi*nr*d/lambda1)^2*((2*deltan*nr-deltan^2)/nr^2);
%kx=146500; %for sample 201-056
kx=2667900; % For sample B

RHS=sqrt(A^2-(kx.*d/2).^2); %Right Hand side of characteristic equation

LHS=(kx.*d/2).*tan(kx.*d/2)*(1-deltan/nr)^2; % Left hand side of characteristic
equation

% Step process to converge on the solution when RHS=LHS.
while abs(RHS-LHS) > 0.1
    if LHS > RHS
        kx=kx-10;
    elseif LHS < RHS
        kx=kx+10;
    end
    RHS=sqrt(A^2-(kx.*d/2).^2);
    LHS=(kx.*d/2).*tan(kx.*d/2)*(1-deltan/nr)^2;
end

```

```

kx=kx+1;
end
RHS=sqrt(A^2-(kx.*d/2).^2);
LHS=(kx.*d/2).*tan(kx.*d/2)*(1-deltan/nr)^2;
end

while abs(RHS-LHS) > 0.001
if LHS > RHS
    kx=kx-0.1;
elseif LHS < RHS
    kx=kx+0.1;
end
RHS=sqrt(A^2-(kx.*d/2).^2);
LHS=(kx.*d/2).*tan(kx.*d/2)*(1-deltan/nr)^2;
end

while abs(RHS-LHS) > 0.0001
if LHS > RHS
    kx=kx-0.01;
elseif LHS < RHS
    kx=kx+0.01;
end
RHS=sqrt(A^2-(kx.*d/2).^2);
LHS=(kx.*d/2).*tan(kx.*d/2)*(1-deltan/nr)^2;
end

while abs(RHS-LHS) > 0.00001
if LHS > RHS
    kx=kx-0.001;
elseif LHS < RHS
    kx=kx+0.001;
end
RHS=sqrt(A^2-(kx.*d/2).^2);
LHS=(kx.*d/2).*tan(kx.*d/2)*(1-deltan/nr)^2;
end

while abs(RHS-LHS) > 0.000001
if LHS > RHS
    kx=kx-0.0001;
elseif LHS < RHS
    kx=kx+0.0001;

```

```
% Once kx is found, it is plugged into the equation for gamma  
kx  
psi=kx*d/2;  
psio=2*pi*nr*d/lambda1;  
top=1+(1-2*psi^2/psio^2)*sin(2*psi)/(2*psi);  
zeta=(1-psi^2/psio^2+RHS^2/psio^2)*(1-deltan/nr)^4*cos(psi)^2/RHS;  
bottom=top+zeta;  
  
gamma=top/bottom;
```

Bibliography

1. Ashley, T. "Type-I InSb-Based Mid-Infrared Diode Lasers," *Philosophical Transactions of the Royal Society London, Series A*, 359(1780):475–488 (February 2001).
2. Bhattacharya, P. *Semiconductor Optoelectronic Devices* (2nd Edition). Prentice Hall, 1997.
3. Burden, R. L. and Faires, J. D. *Numerical Analysis* (3rd Edition). Boston: Prince, Weber and Schmidt, 1985.
4. Casey, H. C. and Panish, M. B. *Heterostructure Lasers*. Part A, Academic Press, Inc., 1978.
5. Choi, H. K. and Turner, G. W. "GaSb-Based Mid-Infrared Quantum-Well Diode Lasers," *SPIE*, 2382:236–243 (1995).
6. Choi, H. K. and Turner, G. W. "InAsSb/InAlAsSb Strained Quantum-Well Diode Lasers Emitting at 3.9 μm ," *Applied Physics Letters*, 67(3):332–334 (July 1995).
7. Choi, H. K., Turner, G. W., Connors, M. K., Herrmann, F. P., Baliga, A., and Anderson, N. G. "InAsSb/InAlAsSb Quantum-Well Diode Lasers Emitting Beyond 3 μm ," *SPIE*, 2682:234–240 (1996).
8. Choi, H. K., Turner, G. W., and Manfra, M. J. "High CW power 200mW/facet at 3.4 μm from InAsSb/InAlAsSb strained quantum well diode lasers," *Electronics Letters*, 32(14):1296–1297 (July 1996).
9. Choi, H. K., Turner, G. W., Manfra, M. J., and Connors, M. K. "175 K Continuous Wave Operation of InAsSb/InAlAsSb Quantum-Well Diode Lasers Emitting at 3.5 μm ," *Applied Physics Letters*, 68(21):2936–2938 (May 1996).
10. Choi, H. K., Turner, G. W., and Le, H. Q. "InAsSb/InAlAs Strained Quantum-Well Lasers Emitting at 4.5 μm ," *Applied Physics Letters*, 66(26):3543–3545 (June 1995).
11. Coherent, , "Mode-Master Beam Propagation Analyzer." User Manual, Software Release 2.0, 1992.
12. Cooley, W. T., Hengehold, R. L., Yeo, Y. K., Turner, G. W., and Loehr, J. P. "Recombination Dynamics in InAsSb Quantum-Well Diode Lasers Measured Using Photoluminescence Upconversion," *Applied Physics Letters*, 73(20):2890–2892 (November 1998).
13. Eliseev, P. G. "Waveguide Optics of New Short-Wavelength Laser Diodes," *SPIE*, 4354:12–23 (2001).

14. Eliseev, P. G. and Drakin, A. E. "Analysis of the Mode Internal Coupling in InGaAs/GaAs Laser Diodes," *Laser Physics*, 4(3):485–492 (1994).
15. Eliseev, P. G., Smolyakov, G. A., and Osinski, M. "Ghost Modes and Resonant Effects in AlGaN-InGaN-GaN Lasers," *IEEE Journal of Selected Topics in Quantum Electronics*, 5(3):771–779 (May/June 1999).
16. Fenimore, D. L., Schepler, K. L., Ramabadran, U. B., and McPherson, S. R. "Infrared Corrected Sellmeier Coefficients for Potassium Titanyl Arsenate," *Journal of the Optics Society of America B*, 12(5):794 (May 1995).
17. Ferguson, E. Personal Communication, 2003. Air Force Institute of Technology.
18. Gorski, S. M. *Carrier Dynamics in Mid-Infrared Quantum Well Lasers Using Time-Resolved Photoluminescence*. MS thesis, Air Force Institute of Technology, March 2002.
19. Hakki, B. W. and Paoli, T. L. "Gain Spectra in GaAs Double-Heterostructure Injection Lasers," *Journal of Applied Physics*, 46(3):1299–1306 (March 1975).
20. Joulli, A. "New Developments in Mid-Infrared Sb-Based Lasers," *Journal de Physique IV*, 9:Pr2–79–Pr2–96 (1999).
21. Kamiyama, S., Uenoyama, T., Mannoh, M., Ban, Y., and Ohnaka, K. "Theoretical Analysis of Valence Subband and Structures and Optical Gain of GaInP/AlGaInP Compressive Strained-Quantum Wells," *IEEE Photonics Technology Letters*, 4(4):439–441 (April 1993).
22. Kaspi, R., Ongstad, A., Dente, G. C., Chavez, J., Tilton, M. L., and Gianardi, D. "High Power and High Brightness from an Optically Pumped InAs/InGaSb Type-II Midinfrared Laser with Low Confinement," *Applied Physics Letters*, 81(3):406–408 (July 2002).
23. Kaspi, R., Ongstad, A., and Tilton, M. AFRL/DE Kirtland AFB, NM. Personal Communications, 2003.
24. Lane, B., Wu, D., Rybaltowski, A., Yi, H., Diaz, J., and Razeghi, M. "Compressively Strained Multiple Quantum Well InAsSb Lasers Emitting at 3.6 μm Grown by Metal-Organic Vapor Deposition," *Applied Physics Letters*, 70(4):443–445 (January 1997).
25. Mahr, H. and Hirsch, M. D. "An Optical Up-Conversion Light Gate with Picosecond Resolution," *Optical Communications*, 13(2):96 (February 1975).
26. Marciak, M. A., "OENG 651 Optical Diagnostics Lab." Class Notes, Summer Quarter 2002. Air Force Institute of Technology.
27. Mikhailova, M. P. and Titkov, A. N. "Type II heterojunctions in the GaInAsSb/GaSb System," *Semiconductor Science and Technology*, 9:1279–1295 (April 1994).

28. Nick Holonyak, J., Koblas, R. M., and Dupuis, R. D. “Quantum-Well Heterostructure Lasers,” *IEEE Journal of Quantum Electronics*, *QE-16*(2):170–185 (February 1980).
29. Polykov, A. Y., Milnes, A. G., Govorkov, A. V., Druzhinina, L. V., Tunitskaya, I. V., and Smirnov, N. B. “Band Offsets in Heterojunctions of InGaAsSb/AlGaAsSb,” *Solid-State Electronics*, *38*(2):525–529 (1995).
30. Saleh, B. and Teich, M. *Fundamentals in Photonics*. John Wiley and Sons, Inc., 1991.
31. Sanders Press Release, “New Laser Portends Breakthrough In Directable IRCM Systems.” Excerpt from unpublished article. http://www.iews.na.baesystems.com/business/00_news/sa1827.htm, July 2000.
32. Schlereth, K.-H. and Tacke, M. “The Complex Propagation Constant of Multilayer Waveguides: An Algorithm for a Personal Computer,” *IEEE Journal of Quantum Electronics*, *26*(4):627–630 (April 1990).
33. Shah, J. “Ultrafast Luminescence Spectroscopy Using Sun Frequency Generation,” *IEEE Journal of Quantum Electronics*, *QE-24*(2):276–288 (February 1988).
34. Stath, N., Hrle, V., and Wagner, J. “The Status and Future Development of Innovative Optoelectronic Devices Based on III-Nitrides on SiC and on III-Antimonides,” *Material Science and Engineering*, *B80*(1-3):224–231 (March 2001).
35. Turner, G. W., Choi, H. K., and Le, H. Q. “Growth of InAsSb Quantum Wells for Long-Wavelength (4 μm) Lasers,” *Journal of Vacuum Science and Technology B*, *13*(2):699–701 (Mar/Apr 1995).
36. Turner, G. W., Goyal, A. K., Manfra, M. J., Foti, P. J., and Sanchez, A. “Recent Progress in Optically-Pumped, Aluminum-Free Mid-IR Semiconductor Lasers Based on Integrated Absorber Designs,” MIR6
37. Verdeyen, J. T. *Laser Electronics* (3rd Edition). Solid State Physical Electronics, Upper Saddle River, NJ 07458: Prentice Hall, 1995.
38. Vurgaftman, I., Meyer, J. R., and Ram-Mohan, L. R. “Band Parameters for III-V Compound Semiconductors and their Alloys,” *Applied Physics Review*, *89*(11):5815–5875 (June 2001).
39. Wilk, A., Fraisse, B., Christol, P., Boissier, G., Grech, P., Gazouli, M. E., Rouillard, Y., Baranov, A. N., and Joulli, A. “MBE growth of InAs/InAsSb/InAlAsSb ‘W’ Quantum Well Laser Diodes Emitting Near 3 μm,” *Journal of Crystal Growth*, *227-228*:586–590 (2001).

40. Yang, M. J., Meyer, J. R., Bewley, W. W., Felix, C. L., Vurgaftman, I., Barvosa-Carter, W., Whitman, L. J., Bartolo, R. E., Stokes, D. W., Lee, H., and Martinelli, R. U. "Type-II Antimonide Quantum Wells for Mid-Infrared Lasers," *Optical Materials*, 17(1-2):179–183 (June-July 2001).
41. Yariv, A. and Yeh, P. *Optical Waves in Crystals*. New York: Wiley Interscience, 1984.

Vita

Lieutenant Gabriel D. Mounce graduated from Carlsbad High School in Carlsbad, New Mexico. He entered undergraduate studies at New Mexico State University in Las Cruces, New Mexico where he graduated with honors with a Bachelor of Science degree in Electrical Engineering in May 1999. He was commissioned through the AFROTC, Detachment 505 at New Mexico State University.

His first assignment was to Tinker AFB in June 1999 as a project engineer for automated test equipment used in the repair of avionics for multiple Air Force weapon systems. In August 2002, he entered the Graduate School of Engineering and Management, Air Force Institute of Technology. Upon, graduation he will be assigned to the Air Force Research Lab, Rome Site.

REPORT DOCUMENTATION PAGE				<i>Form Approved OMB No. 074-0188</i>
<p>The public reporting burden for this collection of information is estimated to average 1 hour per response, including the time for reviewing instructions, searching existing data sources, gathering and maintaining the data needed, and completing and reviewing the collection of information. Send comments regarding this burden estimate or any other aspect of the collection of information, including suggestions for reducing this burden to Department of Defense, Washington Headquarters Services, Directorate for Information Operations and Reports (0704-0188), 1215 Jefferson Davis Highway, Suite 1204, Arlington, VA 22202-4302. Respondents should be aware that notwithstanding any other provision of law, no person shall be subject to a penalty for failing to comply with a collection of information if it does not display a currently valid OMB control number.</p> <p>PLEASE DO NOT RETURN YOUR FORM TO THE ABOVE ADDRESS.</p>				
1. REPORT DATE (DD-MM-YYYY) 25-03-2003		2. REPORT TYPE Master's Thesis		3. DATES COVERED (From – To) Aug 2002 – Mar 2003
4. TITLE AND SUBTITLE Building Blocks For Time-Resolved Laser Emission In Mid-Infrared Quantum Well Lasers			5a. CONTRACT NUMBER 5b. GRANT NUMBER 5c. PROGRAM ELEMENT NUMBER SN-AFIT-00-05	
6. AUTHOR(S) Mounce, Gabriel, D., 1st Lieutenant, USAF			5d. PROJECT NUMBER 5e. TASK NUMBER 5f. WORK UNIT NUMBER	
7. PERFORMING ORGANIZATION NAMES(S) AND ADDRESS(S) Air Force Institute of Technology Graduate School of Engineering and Management (AFIT/EN) 2950 Hobson Way, Building 640 WPAFB OH 45433-7765			8. PERFORMING ORGANIZATION REPORT NUMBER AFIT/GE/ENP/03-01	
9. SPONSORING/MONITORING AGENCY NAME(S) AND ADDRESS(ES) AFRL/DELS Attn: Dr. Andrew Ongstad 3550 Aberdeen Ave. S.E. Kirtland AFB NM 87117-5776			10. SPONSOR/MONITOR'S ACRONYM(S) AFRL/DELS	
			11. SPONSOR/MONITOR'S REPORT NUMBER(S)	
12. DISTRIBUTION/AVAILABILITY STATEMENT APPROVED FOR PUBLIC RELEASE; DISTRIBUTION UNLIMITED.				
13. SUPPLEMENTARY NOTES				
<p>14. ABSTRACT The objective of this research is to improve the performance of mid-infrared semiconductor quantum-well lasers. Lasers operating in the mid-infrared are useful for many Air Force applications which include infrared (IR) countermeasures in particular. Countermeasure applications require lasers that are compact, and able to emit at high powers while operating at room temperature. Limits to power increases are seen in the transverse modal development of laser oscillation. These modes typically form in the waveguiding active region contributing to the laser output. However, competing modes outside of this region also develop when the confining structural layers have the right characteristics. These competing modes may draw power away from the main lasing mode, causing efficiency to drop. Therefore, theoretical models indicate that these "ghost" modes should be extinguished. The goal of this work is to incorporate antimony-based semiconductor laser devices into a time-resolved photoluminescence (TRPL) experiment to examine modal development immediately after excitation. TRPL utilizes a non-linear wave mixing technique known as frequency upconversion to resolve sub-picosecond luminescence occurrences after excitation. Modification to the experiment is performed to produce laser emission from five mid-IR semiconductor laser samples. Both spontaneous and stimulated emission spectra are recorded. Alignment of the experiment is also carried out to produce upconversion of the PL signal to prepare for the incorporation of laser emission. </p> <p>InAs/InGaSb quantum well laser devices were studied in four categories: dilute and tight waveguide structures, and type-I and type-II energy band geometries. Models are obtained to predict mode development and possible ghost mode resonance in the dilute waveguide case. It is seen here that dilute waveguides generate ghost modes because of the evanescent leakage and subsequent trapping of optical radiation in the cap and substrate layers. This data is then compared to the actual behavior of the samples. Lasing is found to occur in the type-I, tight-waveguide case at low temperatures, while only sub-threshold emission is seen for the type-II dilute-waveguide. This is attributed to the absorption of the optical pump in the GaSb cap layer of the type-II device. Samples having no cap layers to prevent absorption showed only spontaneous emission as was predicted by modelling. The longitudinal mode spacing in emission spectra was measured and found to coincide with calculated values. Gain calculations were also performed using the Fabry-Perot resonances for the samples producing stimulated emission.</p>				
15. SUBJECT TERMS Quantum-Well (QW) Lasers, Antimony-Based Semiconductors, InAs/InGaSb, Infrared Countermeasures, Type-I Quantum-Wells, Type-II Quantum Wells, Dilute Waveguides, Tight Waveguides, Ghost Modes, Modal Development, Modal Resonance, Time-Resolved Photoluminescence (TRPL), Frequency Upconversion.				
16. SECURITY CLASSIFICATION OF:		17. LIMITATION OF ABSTRACT	18. NUMBER OF PAGES	19a. NAME OF RESPONSIBLE PERSON Michael A. Marciniak, LtCol, USAF (ENP)
a. REPORT	b. ABSTRACT	c. THIS PAGE	UU	19b. TELEPHONE NUMBER (Include area code) (937) 255-3636, ext 4529; e-mail: michael.marciniak@afit.edu